minerals

MDPI

Article

The Redefinition of the "Bulunkuole Group" in the West Kunlun Orogenic Belt, Xinjiang (NW China): Implications for Tectonic Evolution of the Proto-Tethys

Mingpeng Ding [1,2], Qiugen Li [3], Haoshu Tang [2,*] and Jing Zhang [1,*]

[1] State Key Laboratory of Geological Processes and Mineral Resources, China University of Geosciences, Beijing 100083, China; dmpedward@163.com
[2] State Key Laboratory of Ore Deposit Geochemistry, Institute of Geochemistry, Chinese Academy of Sciences, Guiyang 550081, China
[3] MOE Key Laboratory of Orogenic and Crustal Evolution, Peking University, Beijing 100871, China; qgli@pku.edu.cn
* Correspondence: tanghaoshu@vip.gyig.ac.cn (H.T.); zhangjing@cugb.edu.cn (J.Z.); Tel.: +86-13688502019 (H.T.)

Abstract: The formation ages and tectonic features of the Bulunkuole Complex (BKC) is critical for understanding the geological evolution of the western section of the West Kunlun Orogenic Belt (WKOB), and they are also critical for understanding the metallogenic background of the Taxkorgan Iron Belt. In this paper, we report new geochemical and in situ zircon U–Pb isotopes data for the most southwestern iron-bearing formation of the BKC. The petrography and sedimentation ages of the BKC reveal that the main part of the BKC was emplaced in the Early to Late Cambrian period as a giant accretionary wedge formed during the Proto-Tethys Ocean south-southwestward subduction. The high-pressure metamorphic rocks located at the margin of the Kangxiwa Fault should be further disintegrated from the Cambrian BKC to form a Triassic accretionary complex. Geochemical characteristics indicate that the metasedimentary rocks of the Cambrian BKC derived predominantly from the regional contemporary intermediate to felsic source rocks, and deposited in the fore-arc basin. Provenance studies further demonstrate that the detrital materials were mainly sourced from the Gondwana-affinity terranes, Mazar Terrane as well as the volcanic and magmatic rocks produced during the Tethys subduction. The metamorphism of the Cambrian BKC occurred at ca. 200 Ma in the western section of the WKOB. Proto-Tethys Ocean did not close until 230 Ma, possibly during the Early Mesozoic (200–180 Ma).

Keywords: West Kunlun orogenic belt; Bulunkuole; Proto-Tethys; zircon U–Pb

check for updates

Citation: Ding, M.; Li, Q.; Tang, H.; Zhang, J. The Redefinition of the "Bulunkuole Group" in the West Kunlun Orogenic Belt, Xinjiang (NW China): Implications for Tectonic Evolution of the Proto-Tethys. *Minerals* **2023**, *13*, 776. https://doi.org/10.3390/min13060776

Academic Editor: János Haas

Received: 10 May 2023
Revised: 31 May 2023
Accepted: 31 May 2023
Published: 6 June 2023

1. Introduction

The West Kunlun Orogenic Belt (WKOB) has a long history of tectonic evolution, particularly Tarim and its adjacent continental blocks. They all witnessed the breakup of the Neoproterozoic Rodinia Supercontinent, the convergence and breakup of the Gondwana Supercontinent in the Cambrian and late Paleozoic, respectively, and the convergence of the Pangea Supercontinent [1,2]. The complex tectonic evolution process and unique tectonic location make it a hotspot for research on the orogenic belt and its early evolution around the Qinghai–Tibet Plateau, as well as a critical location for the study of the Tethys Ocean's tectonic evolution, a subject of long-standing interest to scholars [3–9].

Division of the orogeny belt tectonic units is also essential for regional metallogenic background study. Although numerous researches have been conducted on the partition of the WKOB tectonic units, there are still ambiguities regarding the division of the WKOB's western portion. Based on recent comprehensive investigations into the material composition and structural characteristics of the WKOB [3,10–15], Zhang et al. divided the WKOB into the North Kunlun Terrane (NKT, part of Tarim), the South Kunlun Terrane (SKT), the Mazar and Tianshuihai Terranes (MTTs) (Figure 1a,b). Furthermore, the SKT contains the Taxkorgan Terrane (TXKT) divided by predecessors [16,17]. More than forty iron deposits have been found in this area. They all hosted in the large exposed Bulunkuole Complex (BKC, previously named the Bulunkuole Group) [18] north of Mazar town (Figure 1c). The formation age and tectonic features of the BKC are critical for understanding not only the geological evolution of the WKOB's western section, but also the metallogenic background of the West Kunlun iron belt. The BKC has been the subject of earlier investigations due to its prominence as major ore-bearing strata in the area [19]. However, due to the area's poor natural environment and inconvenient transportation, field geological inquiry has been hampered, and the research degree in the area is relatively weak. The processes responsible for the formation of the BKC remain uncertain. Previous studies on chronology of the BKC (Table 1) range from Neoarchean to Early Paleozoic, while the documented tectonic settings include intracratonic rift, fore-arc basin, and back-arc basin [2,20–23]. The tectonic evolution of the Proto-Tethys in the western part of the WKOB is still unclear [2,17].

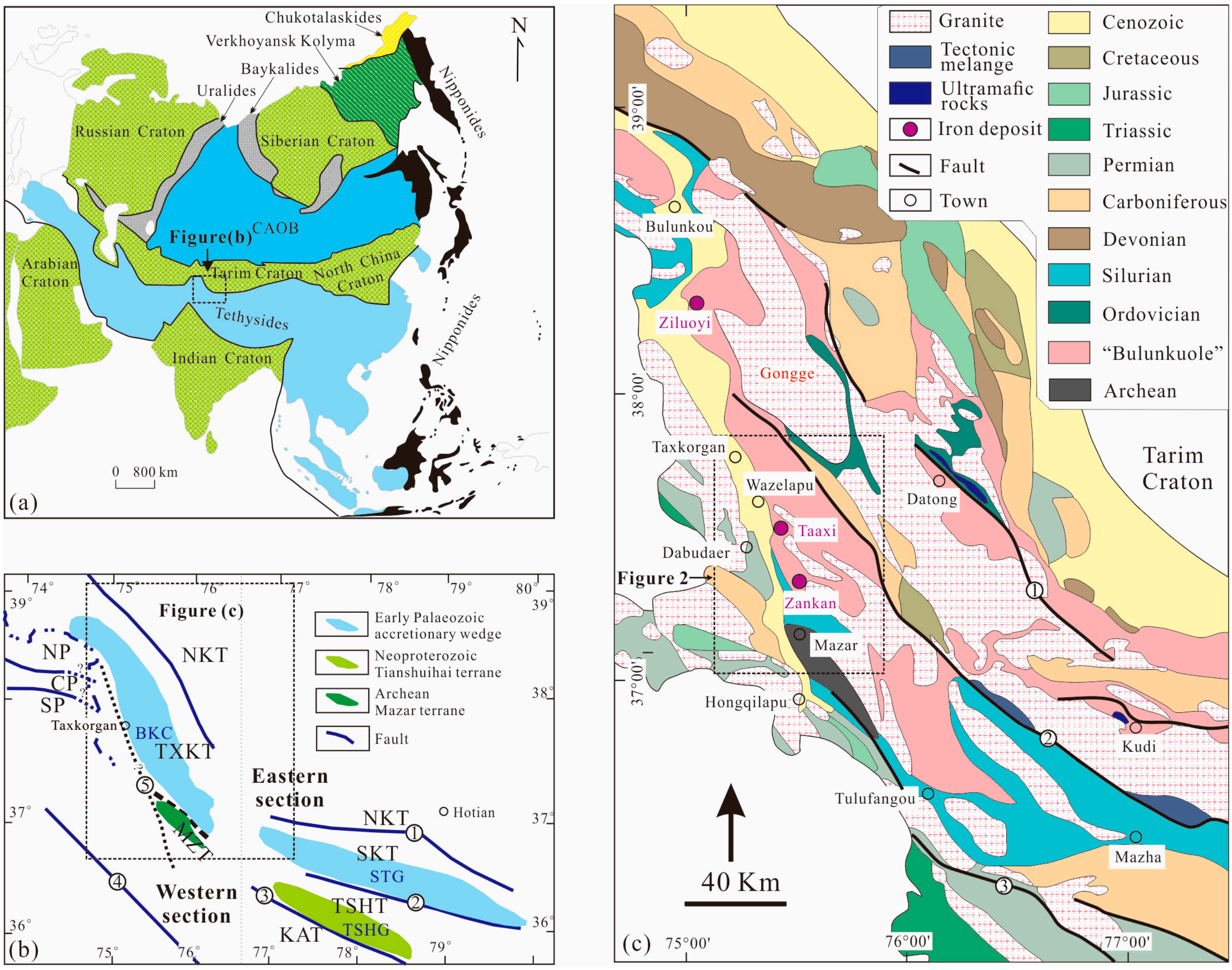

Figure 1. (**a**) Outline of Asian tectonics indicating the location of the western segment of the Himalaya-Tibet Orogenic Belt (after research [4,24,25]; (**b**) Tectonic framework of the West Kunlun Orogenic Belt (WKOB) (after research [17,26]; (**c**) Geological map of the BKC in the WKOB (after research [22]). Abbreviation: CAOB = Central Asian Orogenic Belt; NP = North Pamir; CP = Central Pamir; SP = South Pamir; NKT = North Kunlun Terrane; SKT = South Kunlun Terrane; STG = Setula Group;

BKC = Bulunkuole Complex; TXKT = Taxkorgan Terrane; TSHT = Tianshuihai Terrane; MZT = Archean Mazar Terrane; TSHG = late Neoproterozoic Tianshuihai Group; KAT = Karakorum Terrane. Faults: ① Kudi Fault; ② Kangxiwa Fault; ③ Karakorum Fault; ④ Bangonghu-Nujiang Fault; ⑤ Taxkorgan Fault.

Table 1. Statistical table on the chronology of the Bulunkuole Complex.

Number	Sampling Location	Lithology	Analytical Method	Age/Ma	Age Interpretation	Data Source
1	Bulunkou	Plagioclase gneiss	LA-ICP-MS U-Pb	1828	Magmatic zircon	[27]
2	Bandi	Garnet-biotite schist	SHRIMP U-Pb	2200–600	Detrital zircon	[28]
3	East of Karachigu	Basic volcanic rock	SHRIMP U-Pb	861 ± 43	Magmatic zircon	[29]
4	Dabudaer	Metavolcanic	LA-ICP-MS U-Pb	2481 ± 14	Magmatic zircon	[30]
5	Laobing	Biotite quartzite	LA-ICP-MS U-Pb	532 ± 3.9	Detrital zircon	[31]
6	Laobing	Felsic schist	LA-ICP-MS U-Pb	526 ± 5.0	Detrital zircon	[31]
7	Bulunkou	Quartzite	LA-ICP-MS U-Pb	515/219	Metamorphic zircon	[32]
8	Ziluoyi	Biotite quartz schist	LA-ICP-MS U-Pb	500	Metamorphic zircon	[32]
9	Ziluoyi	Two-mica quartz schist	LA-ICP-MS U-Pb	495	Metamorphic zircon	[32]
10	Zankan	Magnetic iron ore	LA-ICP-MS U-Pb	2465–1959 904–558	Detrital zircon	[32]
11	Zankan	Biotite quartzite	LA-ICP-MS U-Pb	2500 985–706	Detrital zircon	[32]
12	Zankan	Aegirine syenite	LA-ICP-MS U-Pb	551	Magmatic zircon	[32]
13	Zankan	Dacite porphyry	LA-ICP-MS U-Pb	2420–2370 800 2540	Detrital zircon	[33]
14	Zankan	Biotite quartzite	LA-ICP-MS U-Pb	2380 830	Detrital zircon	[33]
15	Yelike	Biotite quartzite	LA-ICP-MS U-Pb	565–517	Detrital zircon	[33]
16	Yelike	Plagioclase gneiss	LA-ICP-MS U-Pb	2600 484	Detrital zircon	[33]
17	Taaxi	Plagioclase amphibole schist	LA-ICP-MS U-Pb	2370	Magmatic zircon	[33]
18	Taaxi	Meta-dacite	LA-ICP-MS U-Pb	521	Magmatic zircon	[34]
19	Bandi	Biotite quartzite	LA-ICP-MS U-Pb	296 ± 2	Magmatic zircon	[35]
20	Taaxi	Plagioclase amphibolite	LA-ICP-MS U-Pb	516.5 ± 5.2	Magmatic zircon	[35]
21	Yelike	Biotite quartzite	LA-ICP-MS U-Pb	473.6 ± 7.4	Metamorphic zircon	[35]
22	Mokaer	Plagioclase amphibole schist	LA-ICP-MS U-Pb	511.2 ± 3.5	Metamorphic zircon	[35]
23	Mokaer	Biotite quartzite	LA-ICP-MS U-Pb	511.7 ± 6.7	Metamorphic zircon	[35]
24	Zankan	Biotite quartzite	LA-ICP-MS U-Pb	2375 ± 81	Magmatic zircon	[36]
25	Zankan	Felsophyre	LA-ICP-MS U-Pb	520 ± 33	Magmatic zircon	[37]
26	Kalaizi	Biotite-plagioclase gneiss	LA-ICP-MS U-Pb	537.2 ± 6.4	Magmatic zircon	[38]
27	Laobing	Felsic gneiss	LA-ICP-MS U-Pb	532 ± 3.9	Detrital zircon	[39]
28	Laobing	Biotite quartzite	LA-ICP-MS U-Pb	526 ± 5.0	Detrital zircon	[39]
29	Bulunkou and north of Laobing	Paragneiss	LA-ICP-MS U-Pb	580/795 (peaks)	Detrital zircon	[2]

Table 1. *Cont.*

Number	Sampling Location	Lithology	Analytical Method	Age/Ma	Age Interpretation	Data Source
30	38°20′45″ N, 74°56′45″ E 37°53′05″ N, 75°16′05″ E 37°53′11″ N, 75°16′01″ E	Metavolcanic	LA-ICP-MS U-Pb	508.1 ± 2.1 515.0 ± 1.7 518.8 ± 2.0	Magmatic zircon	[2]
31	37°53′11″ N, 75°16′01″ E 37°10′25″ N, 75°36′54″ E 37°08′43″ N, 75°32′03″ E 37°53′01″ N, 75°16′08″ E	Gneissic intrusive rocks	LA-ICP-MS U-Pb	510.8 ± 2.1 513.2 ± 3.76 486.1 ± 3.1 245.2 ± 0.98	Magmatic zircon	[2]
32	South of Laobing	Biotite plagioclase granulite	LA-ICP-MS U-Pb	603 ± 10	Magmatic zircon	[40]
33	Jirtiekegou	Biotite-quartz schist	LA-ICP-MS U-Pb	547.4 ± 7.2	Detrital zircon	[20]
34	Zankan	Biotite-quartz schist	LA-ICP-MS U-Pb	2457–2142 1093–737 2643–542	Detrital zircon	[20]
35	Mazar	Intermediate-acid volcanic rock	LA-ICP-MS U-Pb	519–513	Magmatic zircon	[41]
36	Taaxi	Amphibolite	LA-ICP-MS U-Pb	516 ± 6	Magmatic zircon	[42]
37	Zankan	Amphibolite	LA-ICP-MS U-Pb	520 ± 6	Magmatic zircon	[42]
38	Mokear	Amphibolite	LA-ICP-MS U-Pb	516 ± 3	Magmatic zircon	[42]
39	Mazar	Meta-rhyolites	LA-ICP-MS U-Pb	2502.9 ± 7.4	Magmatic zircon	[22]
40	Zankan	Meta-rhyolites	LA-ICP-MS U-Pb	540.2 ± 2.0	Magmatic zircon	[22]
41	Taaxi	Meta-rhyolites	LA-ICP-MS U-Pb	540.2 ± 2.4 530.3 ± 2.5 526.2 ± 3.3 526.2 ± 3.3 515.3 ± 2.3 515.2 ± 2.7	Magmatic zircon	[22]
42	Ziluoyi	Meta-rhyolites	LA-ICP-MS U-Pb	526.4 ± 2.5 516.3 ± 3.9 508.8 ± 3.6	Magmatic zircon	[22]
43	Taaxi	Metavolcanic rocks	LA-ICP-MS U-Pb	539.3 ± 3.3	Magmatic zircon	[21]
44	Yelike	Metavolcanic rocks	LA-ICP-MS U-Pb	543.7 ± 5.7	Magmatic zircon	[21]
45	Yelike	Meta-greywacke	LA-ICP-MS U-Pb	535.9 ± 5.1	Detrital zircon	[21]
46	Kalaizi	Meta-arkose rock	LA-ICP-MS U-Pb	539.7 ± 3.3	Detrital zircon	[21]

In this contribution, we conducted the zircon U–Pb dating, whole-rock geochemistry of the BKC compiled with the published geological and geochemical data to reveal the depositional ages and the geological evolution of the WKOB's western section. Furthermore, the regional metallogenic background was constrained.

2. Geological Background

The WKOB is located at the junction of the India and Tarim Cratons (Figure 1a). Previous studies have divided the WKOB into three parts: North Kunlun Terrane (NKT), South Kunlun Terrane (SKT), and Taxkorgan–Tianshuihai Terrane (TTT) from north to south, which are separated by the Kudi and Kangxiwa Faults, respectively [21,22,43,44]. According to the most recent studies, however, the Taxkorgan Terrane (TXKT) should be considered part of the SKT. The amphibolite- to granulite-facies metamorphic volcanic-sedimentary sequences in the SKT deposited between the Late Sinian and Early Ordovician periods during the southward subduction of the Proto-Tethys Ocean under the MTTs. They exhibit features of typical accretionary complex composing of fore-arc accretion sequences, intraocean arc, arc and ophiolites [16,17].

The TXKT is located in extreme southwest of the WKOB (Figure 1b), bounded by the Kangxiwa Fault to the north and the Taaxi Fault (one fault of the Karakorum Fault Belt) to the south (Figure 2). Lithologies in the TXKT are the BKC and Lower Cretaceous Xialafudi Group and intruded by Proterozoic granodiorite and adamellite, Mesozoic granodiorite and monzonitic granite, and Cenozoic syenogranite, syenite [2,9,16].

The newly discovered Taxkorgan Iron Belt is located in the TXKT (Figure 2) [31,45]. The iron ores, hosted in the metamorphosed volcanic and sedimentary rocks of the BKC (Figure 3), are characterized by an assemblage of magnetite, pyrite and anhydrite (Figure 4h,k). The term "Bulunkuole Group Complex" was initially introduced by the Xinjiang Regional Geological Survey Team in 1967 to encompass a collection of metamorphic complexes found extensively in the Bulunkou and Taxkorgan regions [18]. On the "Geological Map of Western South of Xinjiang at the Scale of 1: 500,000", Wang (1985) named this set of metamorphic rocks the "Bulunkuole Group" [46]. However, with achievements of regional research in the recent decade (Table 1), more and more evidence proves that the previously defined "Bulunkuole Group" is a diachronous complex [47]. Scholars have dissected it and called it the "Bulunkuole Complex" [19,22]. In this contribution, we aim to provide a more detailed analysis and redefinition of the "Bulunkuole Group". As a result, we refer to it as the "Bulunkuole Complex" (BKC) throughout this paper. In China, the BKC is primarily distributed north–south along Gongge Mountain (Figure 1c). It is approximately 200 km long from north to south, 5~50 km wide from east to west, and has an exposed surface of approximately 1500 km^2. Lithologically, the BKC is characterized by a suit of volcanic, clastic, and chemical sedimentary rocks. It was metamorphosed to a greenschist-amphibolite facies and composed of biotite-plagioclase gneiss, plagioclase-amphibole gneissic schist, biotite-quartz schist, schist, magnetite quartzite, meta-siltstone, and marble [30,48]. According to previous studies [29], the lithologic assemblages in the BKC can be divided into four sets of metamorphic assemblages from west to east: the iron-bearing formation, the (garnet) plagioclase-amphibole formation, the sillimanite–garnet gneisses formation, and the marble formation. Based on 1/50,000 mappings and field observations, Zhang et al. (2018) described the rock associations, stratigraphic and metamorphic features in the following three key areas: the Zankan–Laobing iron deposit area (south, Figures 1c and 2), the Wazelapu area (to the south of the high-pressure mafic granulite location, central) and the Ziluoyi iron deposit area (north, Figure 1c) [2]. The most southwestern iron-bearing formation is the primary ore-bearing horizon in the research area. The BKC in this area consists mainly of a series of metamorphic volcanic and sedimentary rocks, with sedimentary rock being the predominant type. According to the regional distribution of rock assemblages, the lower section of the Zankan–Laobing iron deposit area has plagioclase amphibolite and granulite, which are metamorphic products of bimodal volcanic rocks. The upper section is dominated by paragneiss and marble, possibly containing some acid volcanic rocks [17].

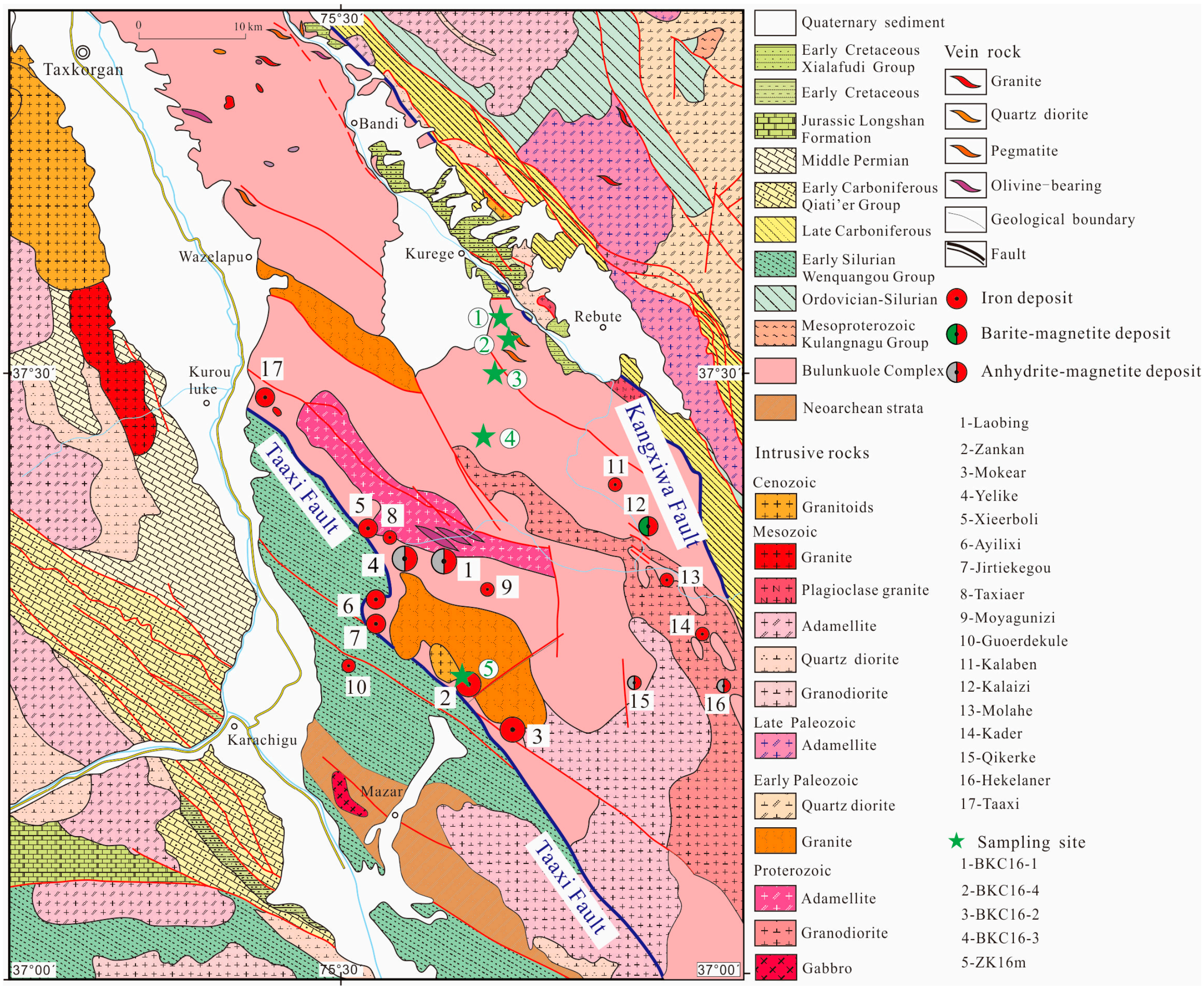

Figure 2. Geological map of the Zankan–Laobing iron deposit area (iron-bearing formation) (after research [20,49]).

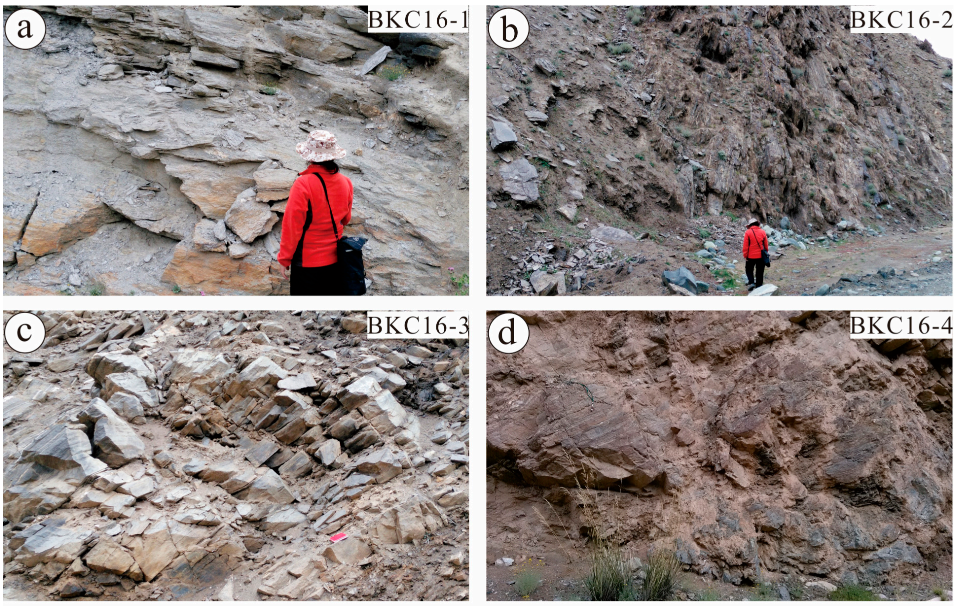

Figure 3. *Cont.*

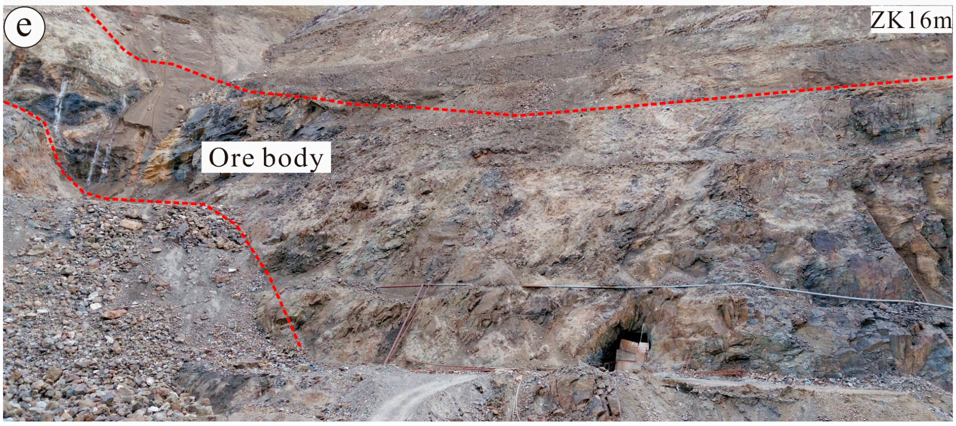

Figure 3. Field photos of the BKC. (**a**) Sillimanite biotite schist/gneiss. (**b**) Garnet-biotite feldspar granulite. (**c**) Biotite-amphibole feldspar schist. (**d**) Plagioclase-amphibolite granulite. (**e**) Garnet-biotite-amphibole quartz schist. The red dashed line is the boundary between the ore body and the host rock.

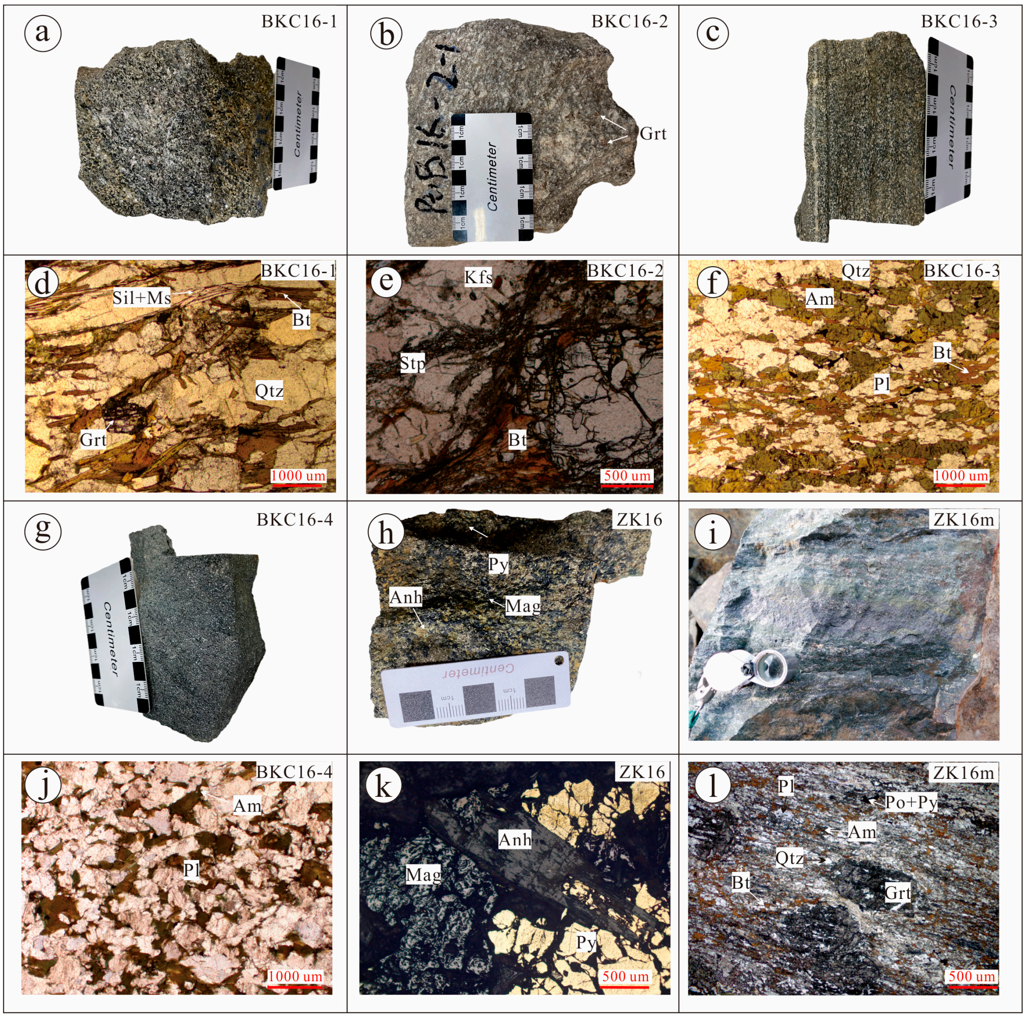

Figure 4. Representative photographs and photomicrographs of rocks from the BKC. (**a**,**d**) Sillimanite-biotite gneiss. (**b**,**e**) Garnet-biotite feldspar granulite. (**c**,**f**) Biotite-amphibole feldspar schist. (**g**,**j**) Plagioclase-amphibolite granulite. (**h**,**k**) Iron ore from the Zankan deposit. (**i**,**l**) The host rock of iron ore bedding from the Zankan deposit (Garnet-biotite-amphibole quartz schist). Abbreviation: Pl = Plagioclase, Kfs = K-feldspar, Qtz = Quartz, Bt = Biotite, Grt = Garnet, Stp = Stilpnomelane, Am = Amphibole, Po = Pyrrhotite, Py = Pyrite, Mag = Magnetite, Anh = Anhydrite, Sil = Sillimanite, Ms = Muscovite.

3. Samples and Methods

3.1. Sample Descriptions

The main rocks in the study area comprise garnet–bearing gneiss, biotite schist, quartzite, biotite-plagioclase-quartz gneiss (meta-rhyolite), amphibolite (meta-basalts), and magnetite layers with minor marble. Geological section survey revealed that the volcanic rocks account for ca. 30% while the sedimentary rocks account for ca. 70% of the thickness. In this study, we collected systematically metasedimentary and metavolcanic rocks of the BKC from five locations (Figures 2–4), and the petrological features of samples are listed in Table 2.

Table 2. Petrological features of the typical rock samples from the BKC.

Sample	Location	Structure	Texture	Lithology	Mineral Assemblage
BKC16-1	37°33′3.366″ N 75°39′41.874″ E	gneissic	medium coarse grain lepidoblastic	Sillimanite-biotite gneiss	sillimanite (~5%), garnet (~5%), biotite (20%), muscovite (~5%), quartz (~60%), and plagioclase (~5%)
BKC16-2	37°30′7.092″ N 75°39′52.884″ E	gneissic	medium to coarse granular-sheet	Garnet-biotite feldspar granulite	garnet (~20%), alkalifeldspar (~20%), plagioclase (~30%), biotite (~10%), amphibole (~10%), quartz (~5%), stilpnomelanite (~5%)
BKC16-3	37°27′11.508″ N 75°39′25.626″ E	schistose	fine to medium granular-sheet	Biotite-amphibole feldspar schist	Plagioclase (~40%), amphibole (~45%), biotite (~10%), quartz (~5%)
BKC16-4	37°22′38.484″ N 75°40′51.276″ E	massive	homoeoblastic	Plagioclase-amphibolite granulit	Plagioclase (~45%), amphibole (~40%), biotite (~5%), quartz (~10%)
ZK16	Zankan iron deposit	massive	granular	Iron ore	Magnetite (~60%), pyrite(~25%),diopside(~10%), apatite, feldspar et al.(~5%)
ZK16m-3 ZK16m-8 ZK16m-9	37°15′2.508″ N 75°37′37.446″ E	schistose	fine grain lepidoblastic	Garnet-biotite amphibole quartz schist	garnet (~10%), biotite (~10%), quartz (~50%), feldspar (~10%), amphibole (mostly anthophyllite~20%), sulfide minerainornor)

3.2. Analytical Methods

3.2.1. Major and Trace Elements

The host rocks of the Zankan iron deposit were selected for major and trace elements analyses at the State Key Laboratory of Ore Deposit Geochemistry, Institute of Geochemistry, Chinese Academy of Sciences (GYIGCAS) in Guiyang. Samples were washed to remove surficial materials and cut to remove weathered surfaces. After that, the fresh rocks were chipped and powdered in an agate puck mill to a fine powder (<200 mesh). Major oxides were analyzed using the ARL Perform'X 4200 X–ray fluorescence (XRF) with analytical uncertainties of 1%–3%. Trace element contents were determined by ICP–MS (Plasma Quant MS Elite) with Relative Standard Deviation (RSD) repeatability test for (most) trace elements < 10%. The specific analysis and testing procedures are referred to [50].

3.2.2. Zircon U–Pb Dating

Zircon grains were concentrated using heavy liquid separation procedures and then handpicked using a binocular microscope after being crushed to 80 mesh. Zircon grains were mounted in epoxy resin and then polished for cathodoluminescence (CL) imaging and laser ablation–inductively coupled plasma–mass spectrometry analysis (LA–ICP–MS).

The IL imaging was undertaken at the Langfang Fengze Source Rock Ore Testing Technology Laboratory. U–Pb dating and trace element analyses of zircon were conducted synchronously by LA–ICP–MS at the State Key Laboratory of Ore Deposit Geochemistry, Institute of Geochemistry Chinese Academy of Sciences. Laser sampling was performed using a GeoLas Pro 193 nm ArF excimer laser. An Agilent 7500x ICP-MS instrument was used to acquire ion-signal intensities. Helium was applied as a carrier gas which was mixed with argon via a T-connector before entering the ICP–MS. Each analysis incorporated a background acquisition of approximately 30 s (gas blank) followed by 60 s of data acquisition from the sample. Offline selection and integration of background and analyte signals, and time drift correction and quantitative calibration for trace element analyses and U–Pb dating were performed by ICPMSDataCal [51,52]. Zircon 91,500 was used as an external standard for U–Pb dating, and it was analyzed twice every 6–8 analyses (i.e., 2 zircon 91,500 + 6–8 samples + 2 zircon 91500). Uncertainty of preferred values for the external standard 91,500 was propagated to the ultimate results of the samples. Concordia diagrams were constructed and weighted mean calculations were conducted using Isoplot [53]. Trace element compositions of zircons were calibrated against multiple-reference materials (NIST 610, BHVO-2G, BCR-2G, BIR-1G) combined with Si internal standardization. The preferred values of element concentrations for the USGS reference glasses were obtained from the GeoReM database (http://georem.mpch-mainz.gwdg.de/ (accessed on 3 September 2018)).

4. Results

4.1. Whole-Rock Geochemistry

The biotite-quartz schists from the Zankan deposit exhibit a homogenous composition, with high concentrations of SiO_2 (60.10–64.99 *wt*%), MgO (2.45–2.98 *wt*%), TFe_2O_3 (7.81–9.56 *wt*%) (Table S1), as well as a moderate amount of TiO_2 + Al_2O_3 (11.11–11.61 *wt*%) and alkali component (Na_2O + K_2O; 4.73–5.24 *wt*%). In the Al_2O_3 v. (Na_2O + K_2O) protolith discriminant diagram, the biotite-quartz schist samples are discriminated into sedimentary rock (Figure 5a). Further, when plotted on the geochemical classification diagram (Figure 5b), the protolith of metasedimentary rocks (TZK29, TZK60) from Li et al. (2019) [20] and our study can be classified into two groups: greywacke and arkose sandstone. Al_2O_3 contents in the meta-greywackes (11.98 *wt*% on average) are lower than those of the upper continental crust (UCC; Al_2O_3 = 15.4 *wt*%, [54]), suggesting a low clay content and distinct source materials for these rocks. In addition, the meta-greywacke samples (5.65 on average) have slightly higher SiO_2/Al_2O_3 ratios than those of igneous rocks (3–5), providing evidence of mildly sedimentary maturation [55].

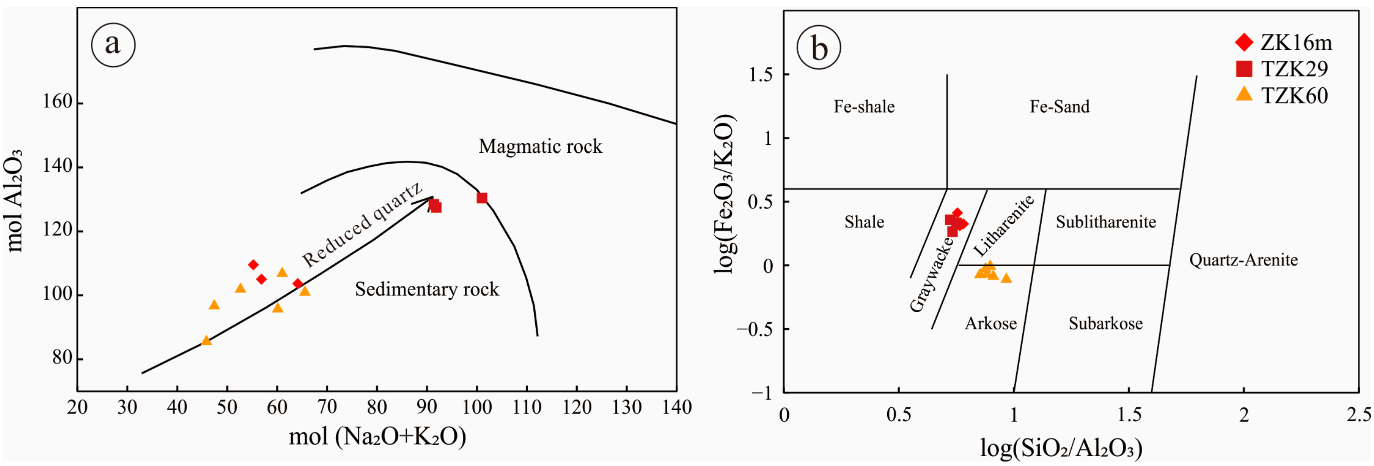

Figure 5. (**a**) Al_2O_3 v. (Na_2O + K_2O) diagram after research [56] of metamorphic rocks in the Zankan area; (**b**) Geochemical classification of the Zankan metasedimentary rocks using the log (SiO_2/Al_2O_3) v. log (TFe_2O_3/K_2O) diagram after research [57]. TZK29 and TZK60 are from [20], similarly hereinafter.

Both meta-greywacke and meta-arkose samples have relatively uniform REE patterns (generally sub-parallel and enriched in the light REE (LREE) (Figure 6a). The heavy REEs (HREE) are weakly fractionated with slightly inclined to flat patterns with $(Gd/Yb)_N$ = 1.28 on average). However, high $(La/Yb)_N$ ratios (3.24–13.0) are observed in all the samples. Moreover, both types of rocks show tiny Ce anomalies (Ce/Ce* = 0.74–1.01). The meta-grey wacke samples have negative Eu anomalies (Eu/Eu* = 0.65–0.73), while the meta-arkose samples possess slightly positive Eu anomalies (Eu/Eu* = 1.05–1.38).

Most schists exhibit similar UCC-normalized trace element patterns for most LILEs (large ion lithophile elements) and HFSEs (high field strength elements) (Figure 6b). Our samples show numerous depletions in Sr and mild enrichments in Th, Ca, P, Y and Tm, and compositions of the other trace elements are comparable with those of UCC. However, for samples from Li et al. (2019) [20], with regard to the large ion lithophile elements (LILEs), Ca and Sr are variably depleted, but K is enriched in all samples. High-field-strength elements (HFSEs), including Hf, Nb, and Ta, are all close to the values of the UCC (Figure 6b). Sr is variably depleted in most samples, implying that plagioclase in the source material of these siliciclastic rocks was decomposed during weathering [58]. The lower or comparable Zr and Hf concentrations and the average Nb/Ta and Zr/Hf ratios (Table S1) similar to those of the UCC suggest that secondary fractionation is negligible, and that there is no preferential accumulation of detrital zircons in these siliciclastic rocks [59–61].

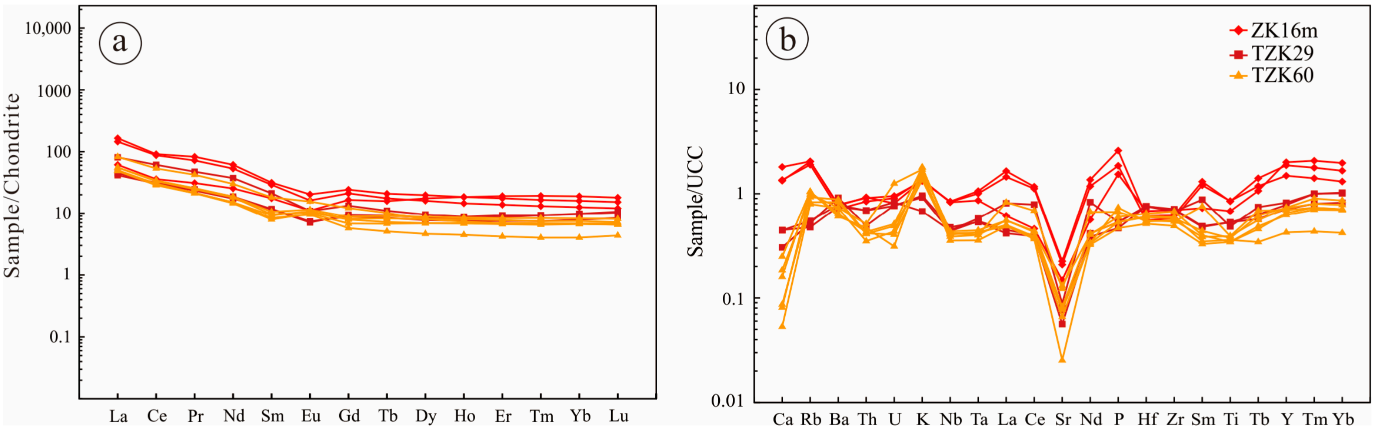

Figure 6. Chondrite-normalized REE patterns (**a**) and upper continental crust (UCC)-normalized spider diagrams (**b**) for metasedimentary rocks. Chondrite normalization after research [62] and UCC normalization after research [54].

4.2. Zircon U–Pb Ages

The zircon U–Pb isotopic data of the representative samples from the Taxkorgan area are present in Table S2.

4.2.1. Ages of the Metavolcanic Rock

Most zircon grains from the meta-andesite sample (BKC16-4) are prismatic, ranging from 50 to 100 μm in length with length/width ratios of 1–2. According to the CL image features, almost all zircon grains display oscillatory zoning characteristic of magmatic zircon (Figure 7). A total of twenty-four analyses were performed on zircons from this sample. These zircons display high Th/U ratios ranging from 0.3 to 0.8, except for point 25, which has suffered intensive metamictization with high uranium contents, and point 11, which is captured zircon.

The zircon grains from meta-andesite yield a narrow range of ages from 509 to 579 Ma (Figure 8a). Four youngest analyses yield consistent results within analytical error and a weighted mean age of 517.9 ± 1.7 Ma. This age is interpreted to the extrusive age of meta-andesite protolith.

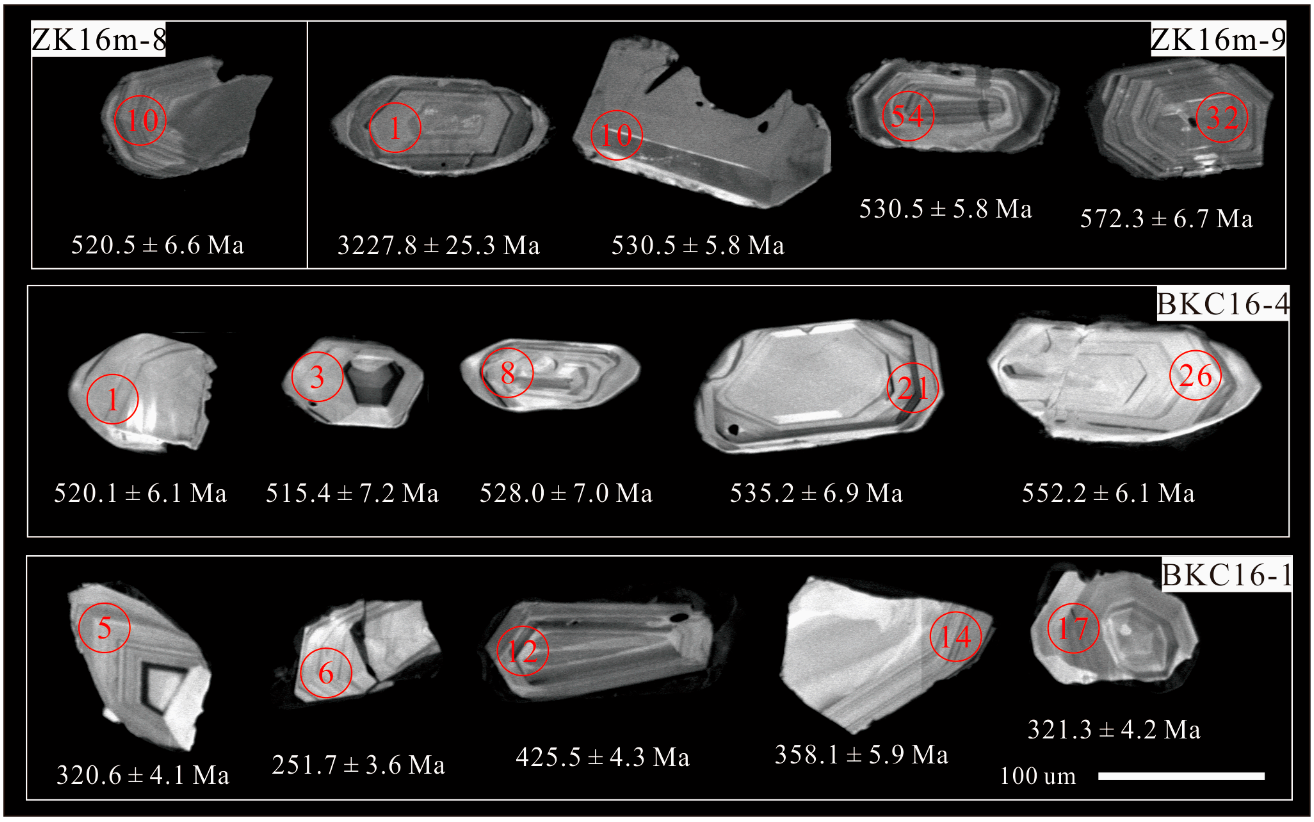

Figure 7. Representative cathodoluminescence images of magmatic zircons and detrital zircons from the BKC (see details in the text). The red circles are U–Pb analytical sites.

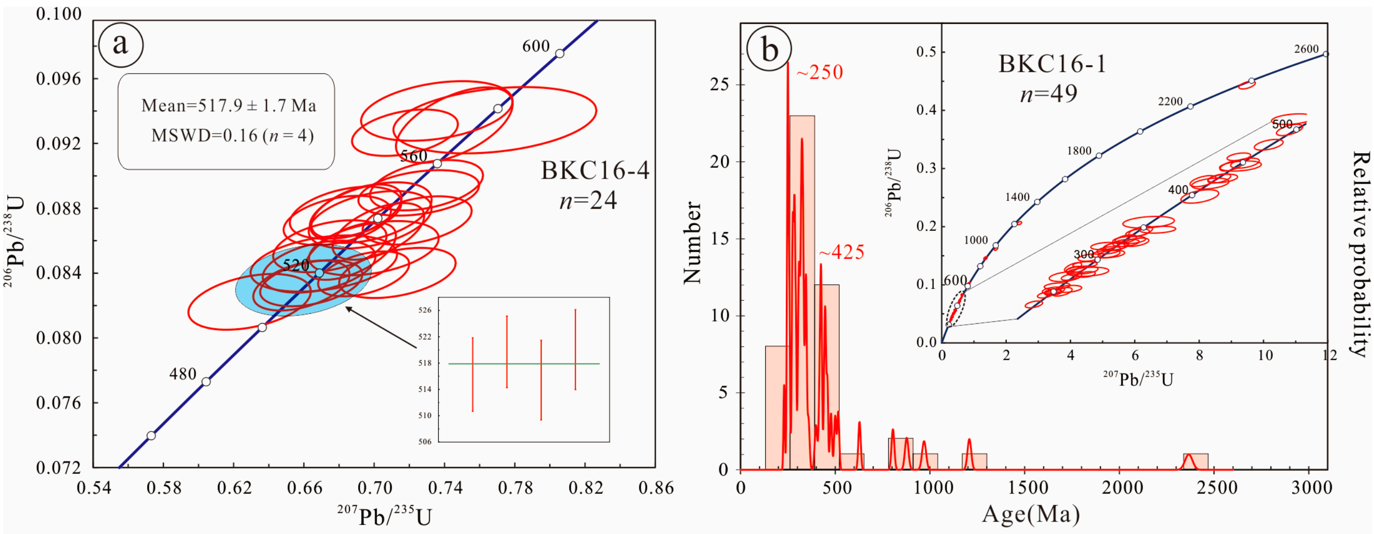

Figure 8. *Cont.*

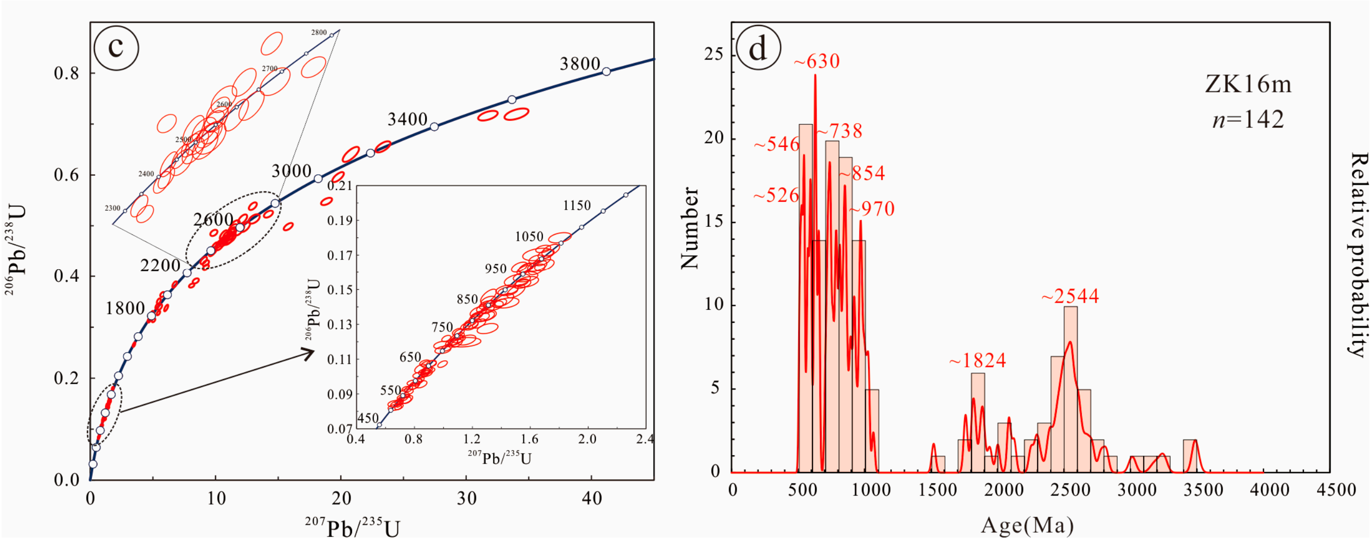

Figure 8. Concordia and combination plot of the zircon U–Pb ages of the metavolcanic rocks ((**a**), BKC16-4) and concordia and combination plot (Histogram + Probability Density Plot, PDP) of the zircon U–Pb ages of the detrital zircons of the metasedimentary samples ((**b**), BKC16-1; (**c**,**d**), ZK16m) from the Taxkorgan area (see details in the text).

4.2.2. Ages of the Metasedimentary Rocks

One hundred and forty-two and forty-nine analyses were obtained from samples ZK16m and BKC16–1, respectively. Detrital zircon grains from these samples share similar characteristics. Most zircons range from 100 μm to 150 μm in length with aspect ratios of 1–2, displaying euhedral or semi-euhedral shapes, suggesting a near-source region; some zircons are oval or round, indicating their long-distance transportation or abrasion, whereas some grains are fragmented with sharp edges. In the CL images, zircon grains show very different inner features with oscillatory zoning, homogenous or wide stripe inner texture, indicating different origins (Figure 7). Most zircons display high Th/U ratios (0.12–2.80) (Table S2), which are typical of igneous origin. A few zircon grains exhibit no zoning, or contain narrow rims with inherited cores, relatively low Th/U ratios (0.01–0.99) and high uranium contents which suggest a metamorphic origin and intensive metamictization (Figure 7). Some samples show radiogenic Pb loss in different degrees (Figure 8b,c).

The detrital zircon grains from BKC16-1 exhibit a wide range of ages from 230 to 2366 Ma (Figure 8b). On the combination plot, two prominent peaks at ca. 250 Ma and 425 Ma are observed, and the youngest zircon grains yield an age of ca. 230 Ma (Figure 8b).

However, detrital zircon grains from the sample ZK16m yield a wide range of ages from 485 to 3494 Ma (Figure 8c). On the combination plot, three prominent peaks at ca. 546 Ma, 630 Ma and 738 Ma are observed (Figure 8d) for the sample ZK16m. These results have revealed the presence of Precambrian components in our survey area, as evidenced by two prominent peaks at ca. 1824 Ma and 2544 Ma. The existence of the Neoarchean zircon age population in our samples is an important finding. Thirteen zircon grains yield a weighted average $^{207}Pb/^{206}Pb$ age of 2514 ± 17 Ma (MSWD = 0.67) (Figure 8c). The youngest set of zircons is concentrated at ca. 526Ma, representing the upper limit deposition age of the samples.

4.2.3. Metamorphic Zircon U–Pb Ages

Zircons obtained from two samples collected from the Bulunkuole Complex (BKC) exhibit characteristics typical of metamorphic zircons, such as their anhedral or round forms, homogeneous and bright CL images (Figure 9c), with their low Th and U contents and Th/U ratios [63] (Table S2). Metamorphic zircons from sample BKC16-2 display bright accretive edges, while those from sample BKC16-3 exhibit fan-shaped zoning (Figure 9c). Forty-nine analyses were conducted on sample BKC16-3, and forty-four analyses were conducted on sample BKC16-2. The metamorphic zircon grains from biotite amphibole feldspar schist sample (BKC16-3) yield younger ages from 175.2 Ma to 207.9 Ma with an average of 18.4 ± 1.3 Ma (Figure 9a,d). There is an older ages range (189.1 Ma to 223.2 Ma) for the garnet-biotite feldspar granulite sample (BKC16-2, Figure 9b). Two groups of metamorphic ages can be identified, 211.1 ± 1.7 Ma (Figure 9e) and 198.2 ± 2.0 Ma (Figure 9f), respectively, suggesting multiple stages of metamorphism.

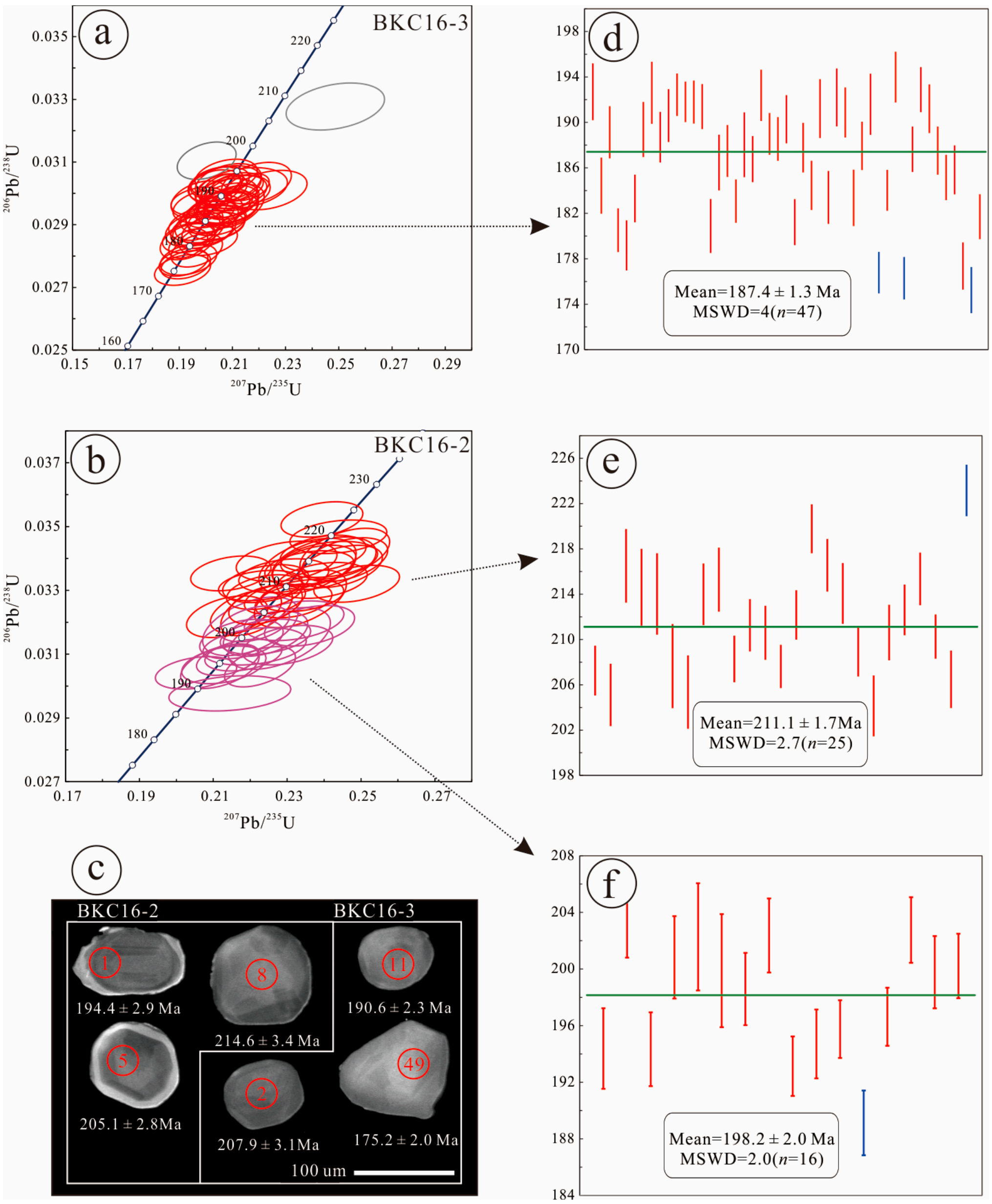

Figure 9. Concordia and weighted average plots of zircon U–Pb ages from metamorphic zircons ((**a**,**d**), BKC16-3, (**b**,**e**,**f**), BKC16-2) from the Taxkorgan area; (**c**) Representative cathodoluminescence images of metamorphic zircons (see details in the text).

5. Discussion

5.1. Geochronology of the BKC

To ascertain the age of the BKC's formation, we compiled the research findings throughout the last two decades (Table 1). The understanding of the formation age and tectonic properties of the BKC can be divided into the following stages: (1) The BKC was formerly considered a Precambrian basement (Bulunkuole Group) of the WKOB owing to its amphibolite-facies metamorphism and the absence of verifiable fossils or isotopic ages [64]. (2) According to the geological survey along the Xinjiang–Tibet Highway, especially the composition of the tectonic mélange belt in the Mazha area (Figure 1c), it was considered that the main body of the tectonic mélange belt belongs to the Triassic system, which was a set of accretive wedge complexes containing the "Bulunkuole Group" in the Taxkorgan area of the west [35]. (3) With the application of high-precision zircon U–Pb isotope dating technology, multiple independent isotope chronological data have been published, where two ages have been proposed: Paleoproterozoic (e.g., [30,32,33,65]) or Early Cambrian (e.g., [20,31,37,66]). A series of Paleoproterozoic metamorphic volcano-sedimentary rocks in the Mazar region have been reported [22,30]. According to Ji et al. (2011) [30], the metamorphic volcanic–sedimentary rocks in this area are part of the BKC. However, a recent study demonstrates that the strata are markedly different from the BKC in terms of material composition, metamorphism, and deformation, and hence should be classified as a separate unit. The Mazar complex was believed to be the only confirmed Early Precambrian rock assemblage of the WKOB [2,9].

Combined with the previous research and our latest data, we provide a new explanation for the age of southern section of the BKC. The U–Pb ages of detrital zircon grains from the biotite-amphibole-quartz schist samples (ZK16m) and the sillimanite-biotite gneiss (BKC16-1) provide a potential means to constrain the depositional ages of the sedimentary sequences and the associated iron deposit. The metamorphic zircons and those with serious Pb loss were removed, and the youngest detrital grains obtained from the samples can be used to constrain their maximum depositional age [67]. In the Zankan area, zircon U–Pb ages of the sample ZK16m constrain the maximum depositional age to ca. 526 Ma, which indicates that the deposition of the Zankan iron deposit continued until at least 526 Ma. In addition, previous reported zircon U–Pb ages of metavolcanic rocks range from 540 Ma to 520 Ma [22,38,66], which proves that the mineralization of iron ore is a long-term process accompanied by accretive wedge. In the northern section of the study area, the age of the plagioclase-amphibolite granulite (meta-andesite) BKC16-4 yields a youngest weighted mean age of 517.9 $\pm$ 1.7 Ma. Significantly, two prominent peaks at ca. 520 Ma and 540 Ma were observed, which may indicate long-term volcanic activities in this region. In northernmost section of the study area, the age of the sillimanite-biotite gneiss BKC16-1 constrain the maximum depositional age to ca. 230 Ma.

The metamorphic grade of the BKC is up to amphibolite-facies and even to high-pressure granulite-facies [43,68,69]. However, the metamorphic age is still debated [70–72]. The metamorphic zircons of two samples (garnet-biotite-feldspar granulite and biotite-amphibole–feldspar schist) in the central section of the study area reveal a metamorphic age of 211–187 Ma (Figure 9) with three stages, which is consistent with recent studies of the high-pressure metamorphic rocks [2,43,69,72].

Collectively, our results confirm that the main part of the BKC is Cambrian in age rather than Paleoproterozoic or Triassic. Furthermore, our research indicates that the metamorphic event associated with the BKC occurred in ca. 200 Ma (e.g., [73]). The high-pressure metamorphic rocks (BKC16-1) should be further disintegrated from the Cambrian BKC to form a Triassic accretionary complex together with the sillimanite–garnet-biotite gneiss in eastern Taxkorgan Town [43,72]. They all belong to the Kangxiwa tectonic zone. The depositional age for the BKC provides a reasonable background to further discuss sediment source characteristic and the genesis of the deposit.

5.2. Provenance of the Metasedimentary Rocks of the BKC

Siliciclastic rocks associated with the Zankan iron deposit have been metamorphosed from greenschist to amphibolite facies, as well as possibly altered and weathered. Thus, it is critical to assess element mobility prior to undertaking any geochemical interpretation [74]. The relatively narrow range of the SiO_2/Al_2O_3 (5.21–9.28) and K_2O/Na_2O ratios (0.42–14.48) for the Zankan metasedimentary rocks (Table S1) suggest negligible silicification and K-metasomatism. Both HFSEs (e.g., Zr, Hf, Ti, Nb, Ta) and REEs in clastic sediments are often considered to be immobile and are suitable for provenance interpretation [75–77].

The Index of Compositional Variability (ICV) was applied to fine-grained sedimentary rocks as a measure of compositional maturity [78], and is defined as

$$\mathrm{ICV} = \left(\mathrm{Fe_2O_3} + \mathrm{K_2O} + \mathrm{Na_2O} + \mathrm{CaO^*} + \mathrm{MgO} + \mathrm{MnO} + \mathrm{TiO_2}\right) / \mathrm{Al_2O_3}\ (\text{Molar proportions}). \quad (1)$$

All the ICV values for metasedimentary rocks of the Zankan are >1 (ICV = 1.03 to 2.41, mean = 1.56), indicating that they are compositionally immature and derived from an active tectonic setting [79].

The most widely used chemical index to ascertain the degree of source-area weathering is the Chemical Index of Alteration (CIA) proposed by [80], and it is defined as

$$\mathrm{CIA} = \left[\mathrm{Al_2O_3} / \left(\mathrm{Al_2O_3} + \mathrm{CaO^*} + \mathrm{Na_2O} + \mathrm{K_2O}\right)\right] \times 100\ (\text{Molar proportions}).$$

In such a formulation, it is necessary to make a correction to the measured CaO content for the presence of Ca in carbonates (calcite, dolomite) and phosphates (apatite). For this study, CaO was corrected for phosphate using P_2O_5 (see details in [81]). The Zankan metasedimentary rocks have lower CIA values ranging from 53 to 65, indicating a relatively low–moderate degree of weathering and consequently indicate cool and/or arid conditions or active tectonic setting in the source area [82]. The A-CN-K system is useful for evaluating fresh rock compositions and examining their weathering trend [83]. The A–CN–K triangular diagram (Figure 10a) demonstrates a weathering trend without K-metasomatism in the metasedimentary samples supported by major element geochemistry (as discussed above). The dashed straight line connecting the samples is stretched to the feldspar joining line, indicating that the parent rock is mostly felsic in composition. The metasedimentary samples from the Zankan area trend towards an idealized biotite composition, indicating the apparent enrichments in K may be attributed to hydrothermal or other alterations aside from weathering [20].

Due to oxidation and uranium loss, sedimentary rocks' Th/U ratios tend to rise with increased weathering [82,84,85]. In the Th/U v. Th diagram (Figure 10b), almost all the Zankan samples display lower Th/U ratios than that of UCC (3.89, [54]), suggesting a negligible degree of weathering which is consistent with interpretations based on the CIA and major elements.

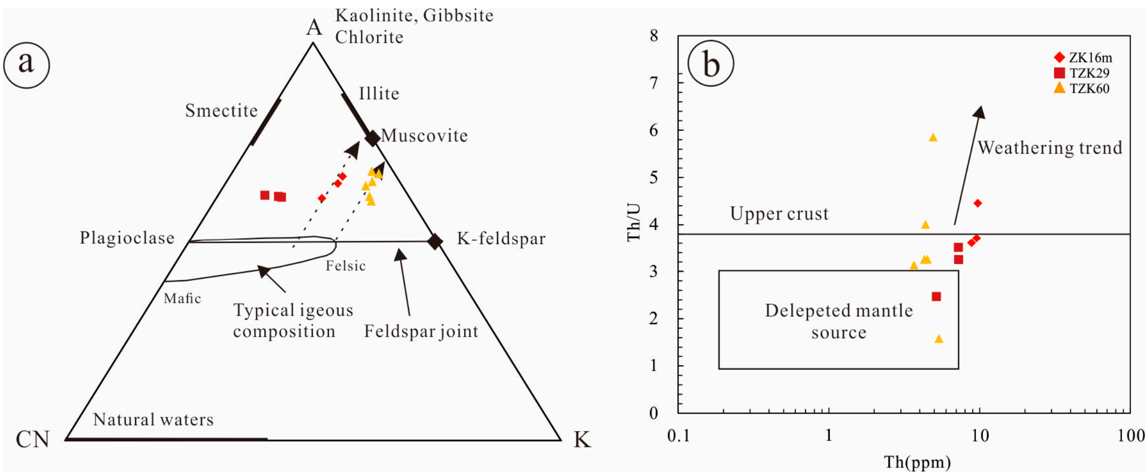

Figure 10. (**a**) Ternary plot of Al_2O_3(A)−CaO* + Na_2O (CN)−K_2O (K) after research [86,87] for the metasedimentary samples. (**b**) Th/U v. Th diagram for metasedimentary rocks from the Zankan iron deposit after research [81].

Another indicator of the source composition is the Al_2O_3/TiO_2 ratio. Feldspars are the primary source of aluminum in normal igneous rocks and the titanium in mafic minerals (e.g., olivine, pyroxene, hornblende, biotite, and ilmenite). Therefore, the Al_2O_3/TiO_2 ratios of igneous rocks generally increase with increasing SiO_2 contents [88]. Sediments with Al_2O_3/TiO_2 values < 14 are likely to be derived from mafic rocks, while sediments with Al_2O_3/TiO_2 values within the 19–28 range might be predominately from a source with average andesitic to rhyodacitic (and/or granodioritic to tonalitic) composition [89]. The Al_2O_3/TiO_2 ratios for the sedimentary rocks range from 19.54 to 47.24, suggesting that they are derived mainly from intermediate-acid rocks.

Additionally, immobile trace elements, such as Zr, Nb, Hf, Ta, Th, U, and Sc, can be used to differentiate between different sedimentary origins [72]. The Zankan schists have La/Sc, Eu/Eu*, Th/U, Zr/Sc and Th/Sc ratios comparable to those of UCC (Table S1), indicating a probable intermediate to felsic igneous source. A plot of Hf against La/Th provides useful bulk rock discrimination between different source compositions [90]. In Figure 11a, the data disperse along the mixed felsic and basic sources and trend to an andesitic arc source, suggesting that they may derive from the mixture of basic and felsic rocks.

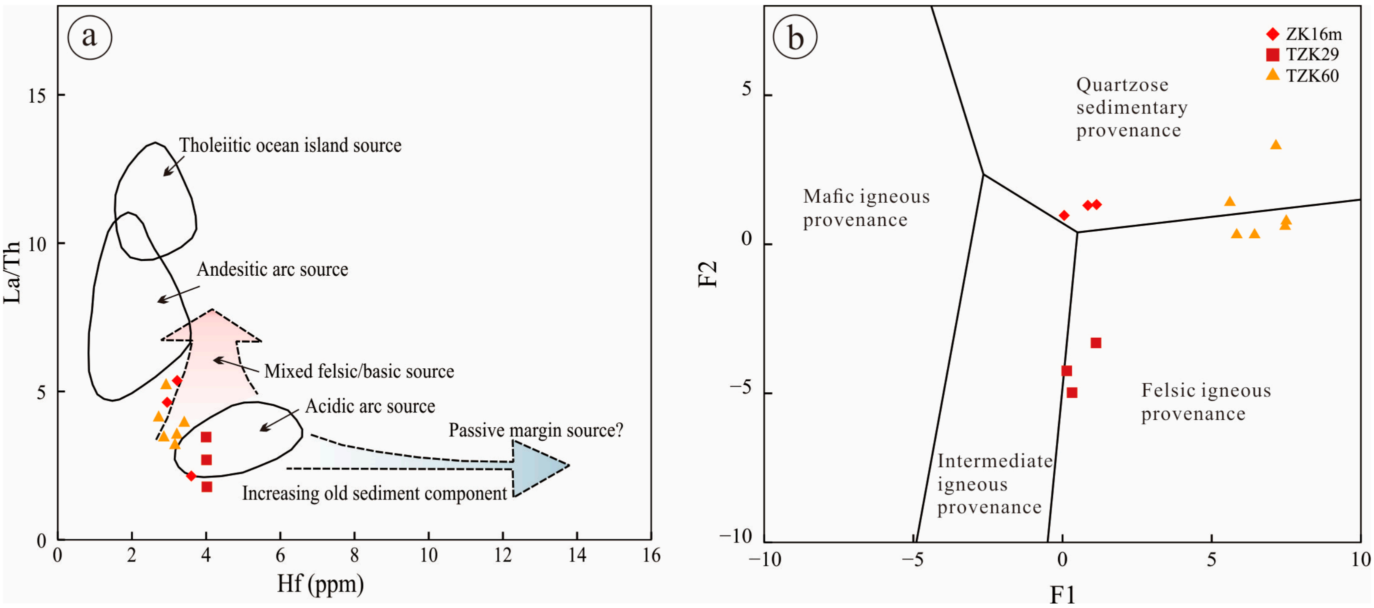

Figure 11. Geochemical diagrams showing the composition of source rocks for the Zankan metasedimentary rocks. (**a**) La/Th v. Hf (ppm) diagram (after research [90]); (**b**) F1 v. F2 diagram (after research [91]. $F1 = -1.773 \times TiO_2 + 0.607 \times Al_2O_3 + 0.76 \times TFe_2O_3 - 1.5 \times MgO + 0.616 \times CaO + 0.509 \times Na_2O - 1.22 \times K_2O - 9.09$, $F2 = 0.445 \times TiO_2 + 0.07 \times Al_2O_3 - 0.25 \times TFe_2O_3 - 1.142 \times MgO + 0.438 \times CaO + 1.475 \times Na_2O + 1.426 \times K_2O - 6.861$.

Discriminant function diagrams based on the abundance of major elements can be used to denote the provenance of sedimentary rocks [91]. In the discriminant function diagram of major element provenance (Figure 11b), most of the samples plot in the provenance region assigned to felsic igneous and quartzose sedimentary, indicating a significant igneous contribution to the Zankan area.

In view of their stability during weathering, transport, diagenesis, and low to medium grade metamorphism, REEs patterns are generally accepted as one of the most reliable indicators of sediment provenance [75]. Typically, mafic rocks contain low REE concentrations and insignificant or no negative Eu anomaly, whereas felsic rocks contain higher REE concentrations and a noticeable negative Eu anomaly [92]. All the Zankan samples show moderate to high ΣREE abundances (63.36–202.39 ppm) and are characterized by fractionated REE with almost flat HREE patterns (Figure 6a). These patterns are comparable to that observed in Early Paleozoic granite, meta-dacite and meta-dacites [21,41], indicating intermediate to felsic source rocks.

Detrital zircon age spectra are also a powerful tool for interpreting the provenance of sedimentary rocks [93]. The studied meta-arenite samples are dominated by a large population of zircons of Pan-Africa age with secondary populations at ~1.82 and 2.54 Ga (Figure 8d). Numerous zircons have ages consistent with those of granites, meta-dacites and meta-rhyolites [21] in the region, showing that felsic igneous rocks are a significant source of metasedimentary materials. Zhang et al. (2018) reported that the Neoarchean metamorphic volcanic–sedimentary sequence of the MZT was deposited at ca.2.5 Ga [9]. This age is consistent with Neoarchean zircon age population of our samples. Hu et al. (2016) reported the detrital zircon U–Pb ages on the marbles and schists of the TSHT, which displayed a similar distribution of age populations with ours, but lacked early Paleozoic records [94]. The possible source for this detritus of the Cambrian BKC was the Gondwana-affinity terranes, such as Lhasa Terrane, South Qiangtang Terrane, and the MZT. Additionally, the volcanic and magmatic rocks produced during the Tethys subduction are also significant contributors [2,26].

5.3. Implication for Tectonic Setting and Tectonic Evolution of the BKC

It has been recognized that there is a magmatic arc zone related to the southward subduction of the Proto-Tethys Ocean in the northern margin of the MTTs [26,41,42,95], while the tectonic setting of the BKC is still controversial, including the intracratonic rift, fore-arc basin, and back-arc basin.

There is a strong correlation between the tectonic setting of depositional basins and the geochemical features of the sediments [96]. However, considering the different tectonic backgrounds of different source areas, geochemical criteria must be utilized cautiously [97]. In general, there is a progressive decrease in TFe_2O_3 + MgO, TiO_2, and Al_2O_3/SiO_2 ratios, and an increase in Al_2O_3/(CaO + Na_2O) in sandstones from the oceanic island arc to the continental island arc to active continental margins to passive margins [98]. The Zankan metasedimentary samples have moderate TFe_2O_3 + MgO (4.33–12.54 *wt*%), Al_2O_3/SiO_2 ratios (0.11–0.19) and relatively TiO_2 contents (0.22–0.55), which shares geochemical affinities with continental arcs or active continental margin settings. In view of the fact that the area has experienced a long period of metamorphic deformation and weathering effects, immobile elements such as Th, Sc, and Zr are more useful in distinguishing tectonic environments than the major elements. The most appropriate tectonic discriminatory plots are compiled to apply for the graywacke. In the Th-Sc-Zr/10 and Ti/Zr v. La/Sc diagrams [96] (Figure 12), most of the samples plot in the field of continental island arc and active continental margin setting [99]. Given the abundance of older detrital zircon grains in the metasedimentary rock samples, the intra-arc deposition was largely ruled out. So, was it the fore-arc or the back-arc?

Significantly, both regional geology and geochemistry favor the theory that the gabbros and gabbroic sheets of the lower BKC are most likely formed in a fore-arc setting [26]. The Early Cambrian BKC is mainly a volcanic–clastic deposit with ophiolite assemblages, and its provenance is mainly arc magmatic material of the early Paleozoic period (Figure 1c), which is consistent with the characteristics of the fore-arc basin. In addition, the geochemical characteristics of sedimentary rocks show the characteristics of continental arcs, which rarely develop back-arc basins with large and thick deposits [100]. Considering the abundance of bimodal volcanic rocks in the region, we suggest that a continental fore-arc extensional basin may be the most suitable.

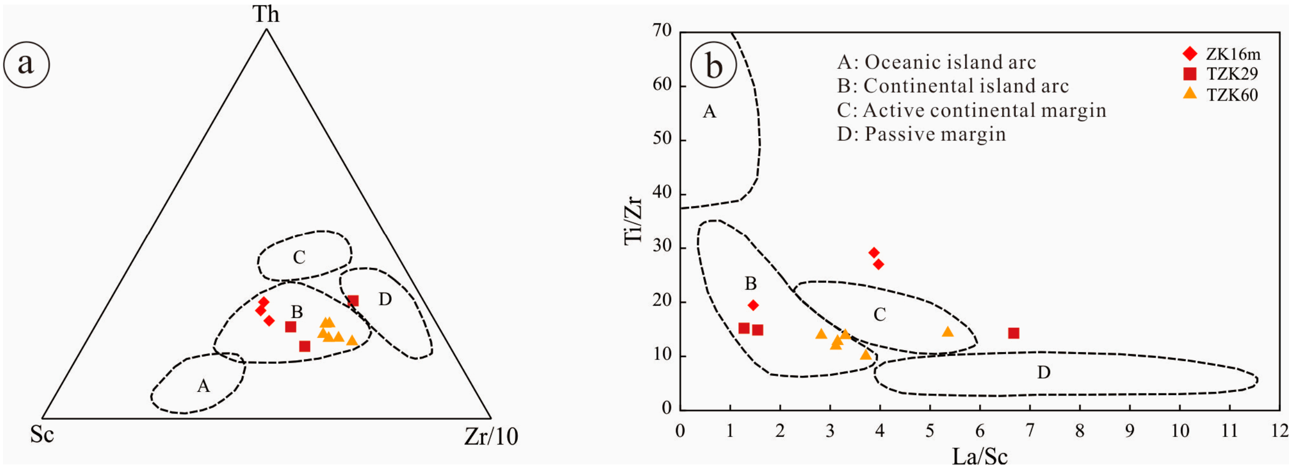

Figure 12. Tectonic discrimination diagrams for the Zankan metasedimentary rocks. (**a**) Th-Sc-Zr/10 diagram (after research [96]); (**b**) Ti/Zr v. La/Sc discrimination plots (after research [96]).

Collectively, we established a possible tectonic evolution model of the Early Cambrian BKC to constrain the iron ore mineralization in the region (Figure 13). In this model, we regard the BKC in the western section of the WKOB as a giant accretionary wedge between the Tarim and MTTs formed during the Proto-Tethys Ocean south–southwestward subduction (present orientation, Figure 13). Based on the age of our sedimentary and volcanic rocks and the early Paleozoic granites (our unpublished data) of the BKC, as well as the data collected (Table 1), we constrained the Proto-Tethys subduction to no later than 540 Ma. Then, a continental arc system was formed, in which I-granites, volcanic rocks, and gabbros were developed in the BKC and the northern margin of the MTTs, and a volcanic–sedimentary sequence was deposited in the fore-arc basin, in which the Taxkorgan Iron Belt was developed.

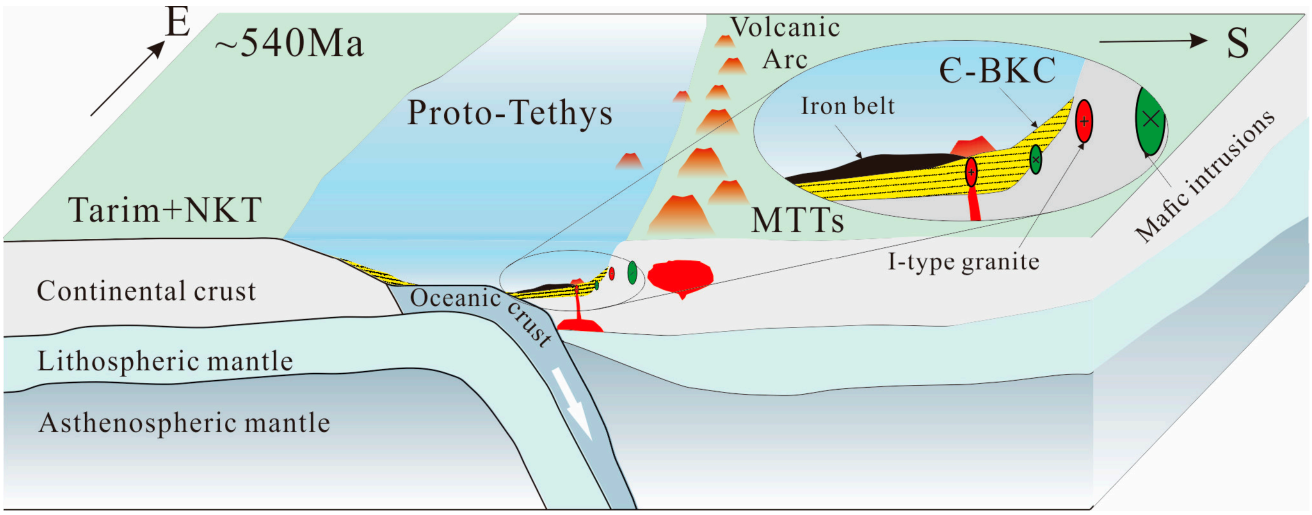

Figure 13. Model of the tectonic evolution of the West Kunlun Orogenic Belt (WKOB) during the Early Cambrian period. Abbreviation: NKT = North Kunlun terrane; MTTs = Mazar–Tianshuihai terranes; Є-BKC = Cambrian Bulunkuole Complex.

The evolution of the eastern WKOB from Proto-Tethys to Paleo-Tethys has been studied in detail [2,16,26]. The southward subduction of the Proto-Tethys Ocean probably started in ca. 540 Ma, which led to the deposition of the SKT (the Setula Group). The collision between the NKT and TSHT occurred during 445~440 Ma, which led to the metamorphism of amphibolite-granulite facies of the Setula Group in this area [101]. Thereafter, the extension began in about 430 Ma and was marked by the emergence of A-type granite in 400 Ma [102,103], representing the end of the Proto-Tethys Ocean evolution. However, subtractive closure time of the Proto-Tethys in the western section of the WKOB is still controversial. Liu et al. (2023) proposed that the early Paleozoic orogenic event in the SKT of the WKOB did not extend to the western section of the WKOB based on the following lines of evidence [104]: (1) Silurian amphibolite-facies metamorphism, concurrent with the Devonian molasse unconformably overlying on the Sinian–Cambrian metamorphic rocks, was well documented in the SKT of the WKOB, whereas no early Paleozoic metamorphism has ever been identified in the western section of WKOB [2]. Instead, our data indicate that the amphibolite- to high-pressure granulite-facies metamorphism of the Cambrian BKC occurred in ca. 200 Ma [72], which is consistent with the absence of late Devonian molasse in the western section of the WKOB. (2) Post-orogenic igneous activity is absent in the western section of the WKOB, indicating its distinct evolution process since ca. 440 Ma. (3) In the northeastern margin of the NE Pamir, continuous late Ordovician to Devonian sedimentary sequences are characterized by shallow marine deposition, and Carboniferous–Permian sequences were mainly platform limestone [105], indicating a continuous ocean evolution. Our new age data (BKC16-1) provide definitive evidence of continued sedimentation at the edge of the TXKT (adjacent to the Kangxiwa Fault, Figure 2) up to 230 Ma, when the Proto-Tethys Ocean was still unclosed. The relic Proto-Tethys was finally closed during the early Mesozoic as recorded by the 211–187 Ma amphibolite- to granulite-facies metamorphism in the BKC [73,101].

6. Conclusions

Based on the detail zircon U–Pb isotopic and whole rock geochemistry data of the BKC in the Taxkorgan area, we draw the following main conclusions:

The main part of the BKC was emplaced in the Early to Late Cambrian period as a giant accretionary wedge formed during the Proto-Tethys Ocean south–southwestward subduction; subsequent metamorphism occurred in ca. 200 Ma.

The high-pressure metamorphic rocks should be further separated from the Cambrian BKC to form a Triassic accretionary complex.

The host rocks, siliciclastic rocks, of the Zankan iron deposit derived predominantly from the regional contemporary intermediate to felsic source rocks with tiny additions of older detritus of the Precambrian crust, and deposited in the fore-arc basin, in which the Taxkorgan Iron Belt was developed.

Provenance studies show that detrital materials of the sediments at Zankan are mainly sourced from the Gondwana-affinity terranes, such as the Lhasa Terrane, the South Qiangtang Terrane, and the Mazar Terrane. Additionally, the volcanic and magmatic rocks produced during the Tethys subduction are also significant contributors.

In the western section of the WKOB, Proto-Tethys did not close until 230 Ma, possibly during the Early Mesozoic period (211–187 Ma).

Supplementary Materials: The following supporting information can be downloaded at: https://www.mdpi.com/article/10.3390/min13060776/s1, Table S1: Whole-rock major (%) and trace (10^{-6}) elements of metasedimentary from the Taxkorgan area; Table S2: The zircon U–Pb isotopic data of the representative samples from the Bulunkuole Complex.

Author Contributions: Funding acquisition, H.T.; Project administration, H.T.; Supervision, J.Z.; Visualization, M.D.; Writing—original draft, M.D.; Writing—review and editing, Q.L. and H.T. All authors have read and agreed to the published version of the manuscript.

Funding: This research was funded by the National Natural Science Foundation of China (Nos. 41672086), National key research and development program (2022YFC2903403), the China Geological Survey Bureau (1212011140056).

Data Availability Statement: The data presented in this study are available on request from the corresponding author.

Acknowledgments: We thank the academic editor and two anonymous reviewers for their constructive suggestions, pertinent comments and careful corrections, which greatly improved the quality of the manuscript. We thank Yanwen Tang, Shuqin Yang and Zhihui Dai helped the laboratory work. Yanjing Chen, Lianhui Dong, Xun Qu, Jihong Li, Changrong Feng and Yanshuang Wu, Bing Xiao, Shuguang Zhang as well as the Geological Survey of Xinjiang helped the field investigation.

Conflicts of Interest: The authors declare no conflict of interest.

References

1. Zhang, C.L.; Zou, H.B.; Li, H.K.; Wang, H.Y. Tectonic framework and evolution of the Tarim Block in NW China. *Gondwana Res.* **2013**, *23*, 1306–1315. [CrossRef]
2. Zhang, C.L.; Zou, H.B.; Ye, X.T.; Chen, X.Y. Tectonic evolution of the NE section of the Pamir Plateau: New evidence from field observations and zircon U-Pb geochronology. *Tectonophysics* **2018**, *723*, 27–40. [CrossRef]
3. Li, S.Z.; Zhao, S.U.; Liu, X.; Cao, H.H.; Yu, S.; Li, X.Y.; Somerville, I.; Yu, S.Y.; Suo, Y.H. Closure of the Proto-Tethys Ocean and Early Paleozoic amalgamation of microcontinental blocks in East Asia. *Earth Sci. Rev.* **2018**, *186*, 37–75. [CrossRef]
4. ŞEngör, A.M.C. The Palaeo-Tethyan suture: A line of demarcation between two fundamentally different architectural styles in the structure of Asia. *Isl. Arc* **1992**, *1*, 78–91. [CrossRef]
5. Tapponnier, P.; Peltzer, G.; Armijo, R. On the mechanics of the collision between India and Asia. *Geo. Soc. Lond. Spec. Pub.* **1986**, *19*, 113–157. [CrossRef]
6. Ducea, M.N.; Lutkov, V.; Minaev, V.T.; Hacker, B.R. Building the Pamirs: The view from the underside. *Geology* **2003**, *31*, 849. [CrossRef]
7. Li, S.Z.; Zhao, S.J.; Li, X.Y.; Cao, H.H.; Liu, X.; Guo, X.Y.; Xiao, W.J.; Lai, S.C.; Yan, Z.; Li, Z.H. Proto-Tethys Ocean in East Asia (I) Northern and southern border faults and subduction polarity. *Acta Petrol. Sin.* **2016**, *32*, 2609–2627, (In Chinese with English abstract).
8. Li, S.Z.; Zhao, S.J.; Yu, S.; Cao, H.H.; Li, X.Y.; Liu, X.; Guo, X.Y.; Xiao, W.J.; Lai, S.C.; Yan, Z.; et al. Proto-Tehtys Ocean in East Asia (II): Affinity and assmbly of Early Paleozoic micro-continental blocks. *Acta Petrol. Sin.* **2016**, *32*, 2628–2644, (In Chinese with English abstract).
9. Zhang, C.L.; Zou, H.B.; Ye, X.T.; Chen, X.Y. A newly identified Precambrian terrane at the Pamir Plateau: The Archean basement and Neoproterozoic granitic intrusions. *Precambrian Res.* **2018**, *304*, 73–87. [CrossRef]
10. Zhu, D.C.; Zhao, Z.D.; Niu, Y.L.; Mo, X.X.; Chung, S.L.; Hou, Z.Q.; Wang, L.Q.; Wu, F.Y. The Lhasa Terrane: Record of a microcontinent and its histories of drift and growth. *Earth Planet. Sci. Lett.* **2011**, *301*, 241–255. [CrossRef]
11. Zhu, D.C.; Zhao, Z.D.; Niu, Y.L.; Dilek, Y.; Mo, X.X. Lhasa terrane in southern Tibet came from Australia. *Geology* **2011**, *39*, 727–730. [CrossRef]
12. Zhu, D.C.; Li, S.M.; Cawood, P.A.; Wang, Q.; Zhao, Z.D.; Liu, S.A.; Wang, L.Q. Assembly of the Lhasa and Qiangtang terranes in central Tibet by divergent double subduction. *Lithos* **2016**, *245*, 7–17. [CrossRef]
13. Kroner, U.; Roscher, M.; Romer, R.L. Ancient plate kinematics derived from the deformation pattern of continental crust: Paleo-and Neo-Tethys opening coeval with prolonged Gondwana–Laurussia convergence. *Tectonophysics* **2016**, *681*, 220–233. [CrossRef]
14. Zhang, K.J.; Zhang, Y.X.; Tang, X.C.; Xia, B. Late Mesozoic tectonic evolution and growth of the Tibetan plateau prior to the Indo-Asian collision. *Earth Sci. Rev.* **2012**, *114*, 236–249. [CrossRef]
15. Zhang, J.X.; Yu, S.Y.; Mattinson, C.G. Early Paleozoic polyphase metamorphism in northern Tibet, China. *Gondwana Res.* **2017**, *41*, 267–289. [CrossRef]
16. Zhang, C.L.; Zou, H.B.; Ye, X.T.; Chen, X.Y. Tectonic evolution of the West Kunlun Orogenic Belt along the northern margin of the Tibetan Plateau: Implications for the assembly of the Tarim terrane to Gondwana. *Geosci. Front.* **2019**, *10*, 973–988. [CrossRef]
17. Zhang, C.L.; Ma, D.H.; Zhu, B.Y.; Ye, X.T.; Qiu, L.; Zhao, H.X.; Liu, X.Q.; Ding, T.; Wang, Q.; Hao, X.S. Tectonic evolution of the Western Kunlun-Karakorum Orogenic Belt and its coupling with the mineralization effect. *Geo. Rev.* **2019**, *65*, 1077–1102, (In Chinese with English abstract).
18. Bureau of Geology and Mineral Resources of Xinjiang Uygur Autonomous Region. *Regional Geology of Xinjiang Uygur Autonomous Region*; Geological Publishing House Beijing: Beijing, China, 1993. (In Chinese)
19. Zhou, Z.J.; Tang, H.S.; Chen, Y.J.; Chen, Z.L. Trace elements of magnetite and iron isotopes of the Zankan iron deposit, westernmost Kunlun, China: A case study of seafloor hydrothermal iron deposits. *Ore Geol. Rev.* **2017**, *80*, 1191–1205. [CrossRef]
20. Li, Z.Q.; Zhang, L.C.; Xue, C.J.; Zhu, M.T.; Zheng, M.T.; Robbins, L.J.; Konhauser, K.O. Genesis of the Neoproterozoic-Early Cambrian banded iron ore-bearing sedimentary rocks in the Jiertieke-Zankan iron ore belt, West Kunlun Orogenic Belt, Xinjiang (NW China). *J. Asian Earth Sci.* **2019**, *173*, 143–160. [CrossRef]
21. Peng, Z.D.; Zheng, M.T.; Wang, C.L.; Zhang, L.C.; Fan, L.G.; Tong, X.X. Constraints on the age and geodynamic setting of the iron formations and anhydrite Fe-(Ba) deposits in the Bulunkuole Group of the Taxkorgan area, NW China. *Ore Geol. Rev.* **2021**, *133*. [CrossRef]
22. Ding, T.; Tan, T.T.; Wang, J.; Zhang, C.L.; Ye, X.T.; Liang, J.; Hao, X.S.; Wu, B. Field and zircon U–Pb geochronological evidence for the occurrence of Cambrian banded iron formations in the West Kunlun Orogenic Belt, China. *Gondwana Res.* **2021**, *98*, 1–16. [CrossRef]

23. Zheng, M.T.; Wang, C.L.; Zhang, L.C.; Shi, Z.B.; Zhu, M.T.; Li, Z.Q.; He, L.D. Geological and geochemical constraints on the origin of the Early Cambrian Kalaizi Fe–Ba deposit in Western Kunlun, NW China. *Ore Geol. Rev.* **2018**, *100*, 347–359. [CrossRef]
24. Şengör, A.; Natal'In, B.; Burtman, V. Evolution of the Altaid tectonic collage and Palaeozoic crustal growth in Eurasia. *Nature* **1993**, *364*, 299–307. [CrossRef]
25. ŞEngör, A.M.C. Paleotectonics of Asia: Fragments of a synthesis. In *The Tectonic Evolution of Asia*; Cambridge University Press: Cambridge, UK, 1996; pp. 486–640.
26. Zhang, C.L.; Zou, H.B.; Ye, X.T.; Chen, X.Y. Timing of subduction initiation in the Proto-Tethys Ocean: Evidence from the Cambrian gabbros from the NE Pamir Plateau. *Lithos* **2018**, *314–315*, 40–51. [CrossRef]
27. Sun, H.T.; Li, C.J.; Wu, H.; Wang, H.J.; Qi, S.J.; Chen, G.M.; Liu, Z.T.; Gao, P. *Overview of Metallogenesis on Western Kunlun*; Geological Publishing House: Beijing, China, 2003; 251p. (In Chinese)
28. Zhang, C.L.; Lu, S.N.; Yu, H.F.; Ye, H.M. Tectonic evolution of the Western Kunlun orogenic belt in northern Qinghai-Tibet Plateau: Evidence from zircon SHRIMP and LA-ICP-MS U-Pb geochronology. *Sci. China Ser. D* **2007**, *50*, 825–835, (In Chinese with English abstract). [CrossRef]
29. Wang, J.P. Geological features and tectonic significance of melange zone in the Taxkorgan area, West Kunlun. *Geol. Bull. China* **2008**, *27*, 2057–2066.
30. Ji, W.H.; Li, R.S.; Chen, S.J.; He, S.P.; Zhao, Z.M.; Bian, X.W.; Zhu, H.P.; Cui, J.G.; Ren, J.G. The discovery of Palaeoproterozoic volcanic rocks in the Bulunkuoler Group from the Tianshuihai Massif in Xinjiang of Northwest China and its geological significance. *Sci. China. Earth. Sci.* **2011**, *41*, 1268–1280, (In Chinese with English abstract). [CrossRef]
31. Yan, C.H.; Chen, C.J.; Cao, X.Z.; Zhang, W.S.; Chen, J.K.; Li, S.P.; Liu, P.D. The discovery of the "Pamir-type" iron deposits in Taxkorgan area of Xinjiang and its geological significance. *Geol. Bull. China* **2012**, *31*, 549–557, (In Chinese with English abstract).
32. Yang, W.Q. The Indosinian Metamorphism, Magmatism and Formation Age of Bunlunkuole Rock Group in Taxkorgan-Kangxiwar Tectonic Belt, Western Kunlun. Ph.D. Thesis, Northwest University: Xi'an, China, 2013; pp. 1–128, (In Chinese with English abstract).
33. Feng, C.R. Geological Features, Mineralization Model and Prospecting of Iron Deposits in Taxkorgan Region, West Kunlun Mountains. Ph.D. Thesis, China University of Geosciences, Beijing, China, 2013; pp. 1–159, (In Chinese with English abstract).
34. Xiao, P.X.; Gao, X.F.; Kang, L.; Xie, C.R. Redefinition and significance of "Bulunkuole Group" in Taxkorgan region, Xinjiang. Annual Meeting of Chinese Geoscience Union, 2014. *Earth Planet. Phys.* **2014**, *5*, 1–121. (In Chinese)
35. Huang, C.Y. Geological Characteristics and Genesis of the Iron Ore Deposit in the Bulunkuole Group, West Kunlun, Xinjiang. Ph.D. Thesis, Guangzhou Institute of Geochemistry Chinese Academy of Sciences, Guangzhou, China, 2014; pp. 1–83, (In Chinese with English abstract).
36. Li, H.Z.; Zhai, M.G.; Zhang, L.C.; Li, Z.Q.; Zheng, M.T.; Niu, J.; Yu, P.P. Study on geochemistry and micro-area characteristics of Paleoproterozoic chemical sedimentary rocks from Zankan area, West Kunlun, China. *Acta Petrol. Sin.* **2016**, *32*, 233–250, (In Chinese with English abstract).
37. Zhang, L.C.; Feng, J.; Dong, L.H.; Zhu, M.T.; Zheng, M.T.; Li, Z.Q.; Hao, Y.H.; Shi, Y.J. Deposit types, origin and metallogenetic regularity of Taxkorgan Iron Ore Belt in West Kunlun. *J. Earth Sci. Environ.* **2016**, *38*, 427–443, (In Chinese with English abstract).
38. Zheng, M.T.; Zhang, L.C.; Shu, M.T.; Li, Z.Q. Geological characteristics, formation age and genesis of the Kalaizi Ba-Fe deposit in West Kunlun. *Earth Sci. Front.* **2016**, *23*, 252, (In Chinese with English abstract).
39. Chen, J.K. Formation Age of Ore-bearing Strata from the Laobing Iron Deposit in Taxkorgan area of Western Kunlun, Xinjiang and Its GeologicalSignificance. *Northwes. Geol.* **2018**, *51*, 105–120, (In Chinese with English abstract).
40. He, C.G.; Wang, S.Y.; Fang, H.B.; Chai, J.Y.; Su, J.C.; Chang, Y.W.; Wang, L.L.; Chen, D.H. Redefination and ore-forming significance of Maeryang Forming, Taxkorgan, Western Kunlun Mountains. *Geo China* **2019**, *46*, 517–536, (In Chinese with English abstract).
41. Zhang, H.S.; Ji, W.H.; Ma, Z.P.; Gao, X.F.; Sun, C.; Hong, J.; Lv, P.R. Geochronology and geochemical study of the Cambrian andesite in Tianshuihai Terrane: Implications for the evolution of the Proto-Tethys Ocean in the West Kunlun-Karakoram Orogenic Belt. *Acta Petrol. Sin.* **2020**, *36*, 257–278, (In Chinese with English abstract).
42. Hu, J.; Huang, C.Y.; Wang, H. U-Pb zircon geochronology and geochemistry of metavolcanics and associated iron ores of the magnetite-rich BIF deposits in the Western Kunlun orogenic belt: Constraints on the depositional age, origin and tectonic setting. *Ore Geol. Rev.* **2020**, *126*, 103751. [CrossRef]
43. Yang, W.Q.; Liu, L.; Cao, Y.T.; Wang, C.; He, S.P.; Li, R.S.; Zhu, X.H. Geochronological evidence of Indosinian (high-pressure) metamorphic event and its tectonic significance in Taxkorgan area of the Western Kunlun Mountains, NW China. *Sci. China Earth Sci.* **2010**, *53*, 1445–1459. [CrossRef]
44. Xiao, W.J.; Windley, B.F.; Liu, D.Y.; Jian, P.; Liu, C.Z.; Yuan, C.; Sun, M. Accretionary Tectonics of the Western Kunlun Orogen, China: A Paleozoic–Early Mesozoic, Long-Lived Active Continental Margin with Implications for the Growth of Southern Eurasia. *J. Geol.* **2005**, *113*, 687–705. [CrossRef]
45. Dong, L.H.; Li, J.H.; Feng, J.; Zhuang, D.Z.; Liu, B.; Li, F.M.; Qu, X.; Jiang, Y.H. The main Achievement and progress of Xinjiang Geology and Mineral Exploration in 2011. *Xinjiang Geol.* **2012**, *30*, 1–4, (In Chinese with English abstract).
46. Wang, Y.Z. *Geological Map of Western South of Xinjiang at the Scale of 1: 500,000, Mineral Chart Manual. No.2 Geological Party of Xinjiang Bureau of Geological and Mineral Resource*; China University of Geosciences Press: Beijing China, 1985. (In Chinese)
47. Zhu, G.; Liu, W.; Wu, G.; Ma, B.; Nance, R.D.; Wang, Z.; Xiao, Y.; Chen, Z. Geochemistry and U-Pb-Hf detrital zircon geochronology of metamorphic rocks in terranes of the West Kunlun Orogen: Protracted subduction in the northernmost Proto-Tethys Ocean. *Precambrian Res.* **2021**, *363*, 106344. [CrossRef]

48. Wang, S.Y.; Peng, S.M.; Ma, R.S.; Zhang, Y.; Lv, J.G.; Bai, G.D.; Xie, C.Y.; Gao, T.; Ren, J.D.; Liu, P.D.; et al. *The People's Republic of China Regional Geological Report: Kuketuluke Map (J43C003002), Taxkorgan Map (J43C003003): Scale 1: 250000*; China Geological Survey: Beijing, China, 2014.
49. Zhou, Z.J.; Tang, H.S.; Wu, Y.S.; Li, Q.G.; Chen, Y.J.; Chen, Z.L. Geology, geochemistry and genesis of the Zankan iron deposit in the West Kunlun Orogen, Xinjiang, China. *Ore Geol. Rev.* **2018**, *100*, 334–346. [CrossRef]
50. Qi, L.; Zhou, M.F.; Gao, J.f.; Zhao, Z. An improved Carius tube technique for determination of low concentrations of Re and Os in pyrites. *J. Anal. At. Spectrom.* **2010**, *25*, 585–589. [CrossRef]
51. Liu, Y.S.; Hu, Z.C.; Gao, S.; Günther, D.; Xu, J.; Gao, C.G.; Chen, H.H. In situ analysis of major and trace elements of anhydrous minerals by LA-ICP-MS without applying an internal standard. *Chem. Geol.* **2008**, *257*, 34–43. [CrossRef]
52. Liu, Y.S.; Hu, Z.C.; Zong, K.Q.; Gao, C.G.; Gao, S.; Xu, J.A.; Chen, H.H. Reappraisement and refinement of zircon U-Pb isotope and trace element analyses by LA-ICP-MS. *Chin. Sci. Bull.* **2010**, *55*, 1535–1546. [CrossRef]
53. Ludwig, K.R. User's manual for isoplot 3.00, a geochronlogical toolkit for microsoft excel. *Berkeley Geochronl. Cent. Spec. Publ.* **2003**, *4*, 25–32.
54. Rudnick, R.L.; Gao, S. 3.01-Composition of the Continental Crust. In *Treatise on Geochemistry*; Holland, H.D., Turekian, K.K., Eds.; Pergamon: Oxford, UK, 2003; pp. 1–64.
55. Roser, B.P.; Cooper, R.A.; Nathan, S.; Tulloch, A.J. Reconnaissance sandstone geochemistry, provenance, and tectonic setting of the lower Paleozoic terranes of the West Coast and Nelson, New Zealand. *N. Z. J. Geol. Geophys.* **1996**, *39*, 1–16. [CrossRef]
56. Qiu, J.X.; Lin, J.Q. *Lithochemistry*; Geological Publishing House: Beijing China, 1991. (In Chinese)
57. Herron, M.M. Geochemical classification of terrigenous sands and shales from core or log data. *J. Sediment. Res.* **1988**, *58*, 820–829.
58. Wang, C.; Zhang, L.; Dai, Y.; Lan, C. Geochronological and geochemical constraints on the origin of clastic meta-sedimentary rocks associated with the Yuanjiacun BIF from the Lüliang Complex, North China. *Lithos* **2015**, *212–215*, 231–246. [CrossRef]
59. Tao, H.; Sun, S.; Wang, Q.; Yang, X.; Jiang, L. Petrography and geochemistry of lower carboniferous greywacke and mudstones in Northeast Junggar, China: Implications for provenance, source weathering, and tectonic setting. *J. Asian Earth Sci.* **2014**, *87*, 11–25. [CrossRef]
60. Wang, C.; Huang, H.; Tong, X.; Zheng, M.; Peng, Z.; Nan, J.; Zhang, L.; Zhai, M. Changing provenance of late Neoarchean metasedimentary rocks in the Anshan-Benxi area, North China Craton: Implications for the tectonic setting of the world-class Dataigou banded iron formation. *Gondwana Res.* **2016**, *40*, 107–123. [CrossRef]
61. Hu, J.; Wang, H.; Wang, M. Provenance and tectonic setting of siliciclastic rocks associated with the Neoproterozoic Dahongliutan BIF: Implications for the Precambrian crustal evolution of the Western Kunlun orogenic belt, NW China. *J. Asian Earth Sci.* **2017**, *147*, 95–115. [CrossRef]
62. Boynton, W.V. Chapter 3-Cosmochemistry of the Rare Earth Elements: Meteorite Studies. In *Developments in Geochemistry*; Henderson, P., Ed.; Elsevier: Amsterdam, The Netherlands, 1984; Volume 2, pp. 63–114.
63. Hoskin, P.W.; Schaltegger, U. The composition of zircon and igneous and metamorphic petrogenesis. *Rev. Mineral. Geochem.* **2003**, *53*, 27–62. [CrossRef]
64. Cui, J.T.; Bian, X.W.; Wang, G.B. Geological composition and evolution of the western Kunlun. *Geol. Shanxi* **2006**, *24*, 1–11, (In Chinese with English abstract).
65. Li, Z.Q.; Zhang, L.C.; Xue, C.J.; Zheng, M.T.; Hao, Y.H.; Shi, Y.J. Geological and geochemical characteristics of Zankan iron deposit in the West Kunlun Mountains. *Chin. J. Geol.* **2015**, *50*, 100–117, (In Chinese with English abstract).
66. Lin, S.K. Study on Geochemistry and Zircon U-Pb Ages of Dacite Porphyry from the Zankan Iron Deposit West Kunlun Area. Master's Thesis, The Kunming Universty of Science and Technology, Kunming, China, 2015; pp. 1–64, (In Chinese with English abstract).
67. Babinski, M.; Boggiani, P.C.; Trindade, R.I.F.; Fanning, C.M. Detrital zircon ages and geochronological constraints on the Neoproterozoic Puga diamictites and associated BIFs in the southern Paraguay Belt, Brazil. *Gondwana Res.* **2013**, *23*, 988–997. [CrossRef]
68. Liu, W.P.; He, W.; Tong, L.X.; Wu, Y.F.; Huang, C.Y.; Hu, J. Geochemical characteristics and metamorphic PT paths of the Bulunkuole Group in Taxkorgan, western Kunlun. *Acta Petrol. Sin.* **2013**, *29*, 923–937, (In Chinese with English abstract).
69. Qu, J.; Zhang, L.; Ai, Y.; Lü, Z.; Wang, J.; Zhou, H.; Wang, S. High-pressure granulite from Western Kunlun, northwestern China: Its metamorphic evolution, zircon SHRIMP U-Pb ages and tectonic implication. *Sci. China Ser. D* **2007**, *50*, 961–971. [CrossRef]
70. Jiang, Y.H.; Jiang, S.Y.; Ling, H.F.; Zhou, X.R.; Rui, X.J.; Yang, W.Z. Petrology and geochemistry of shoshonitic plutons from the western Kunlun orogenic belt, Xinjiang, northwestern China: Implications for granitoid geneses. *Lithos* **2002**, *63*, 165–187. [CrossRef]
71. Ji, W.H.; Han, F.L.; Wang, J.C.; Zhang, J.L. Compositon and geochemistry of the Subashi ophiolitic mélange in the West Kunlun and its geological significance. *Geol. Bull. China* **2004**, *23*, 1196–1201, (In Chinese with English abstract).
72. Qu, J.F.; Zhang, L.F.; Zhang, J.; Zhang, B. Petrology and geochronology on high-pressure pelitic granulite from Bulunkuole complex in West Kunlun and its tectonic implication. *Acta Petrol. Sin.* **2021**, *37*, 563–574, (In Chinese with English abstract).
73. Robinson, A.C.; Ducea, M.; Lapen, T.J. Detrital zircon and isotopic constraints on the crustal architecture and tectonic evolution of the northeastern Pamir. *Tectonics* **2012**, *31*, 1–16. [CrossRef]
74. Rollinson, H.R. *Using Geochemical Data: Evaluation, Presentation, Interpretation*; Routledge: Abingdon, UK, 2014.

75. Taylor, S.R.; McLennan, S.M. *The Continental Crust: Its Composition and Evolution: An Examination of the Geochemical Record Preserved in Sedimentary Rocks*; Blackwell Scientific Publications: Hoboken, NJ, USA, 1985.
76. Mclennan, S.M. Rare earth elements in sedimentary rocks: Influence of provenance and sedimentary processes. *Geochem. Mineral. Rare Earth Elem.* **2018**, *21*, 169–200.
77. Pearce, J.A. A user's guide to basalt discrimination diagrams. In *Trace Element Geochemistry of Volcanic Rocks: Applications for Massive Sulphide Exploration*; Short Course Notes; Geological Association of Canada: St. John's, NL, Canada, 1996; Volume 12, p. 113.
78. Cox, R.; Lowe, D.R.; Cullers, R.L. The influence of sediment recycling and basement composition on evolution of mudrock chemistry in the southwestern United States. *Geochim. Cosmochim. Acta* **1995**, *59*, 2919–2940. [CrossRef]
79. van de Kamp, P.C.; Leake, B.E. Petrography and geochemistry of feldspathic and mafic sediments of the northeastern Pacific margin. *Earth Environ. Sci. Trans. R. Soc. Edinb.* **1985**, *76*, 411–449. [CrossRef]
80. Nesbitt, H.W.; Young, G.M. Early Proterozoic climates and plate motions inferred from major element chemistry of lutites. *Nature* **1982**, *299*, 715–717. [CrossRef]
81. McLennan, S.M. Weathering and Global Denudation. *J. Geol.* **1993**, *101*, 295–303. [CrossRef]
82. Bauluz, B.; Mayayo, M.J.; Fernandez-Nieto, C.; Gonzalez Lopez, J.M. Geochemistry of Precambrian and Paleozoic siliciclastic rocks from the Iberian Range (NE Spain): Implications for source-area weathering, sorting, provenance, and tectonic setting. *Chem. Geol.* **2000**, *168*, 135–150. [CrossRef]
83. Fedo, C.M.; Wayne Nesbitt, H.; Young, G.M. Unraveling the effects of potassium metasomatism in sedimentary rocks and paleosols, with implications for paleoweathering conditions and provenance. *Geology* **1995**, *23*, 921–924. [CrossRef]
84. Partin, C.A.; Bekker, A.; Planavsky, N.J.; Scott, C.T.; Gill, B.C.; Li, C.; Podkovyrov, V.; Maslov, A.; Konhauser, K.O.; Lalonde, S.V.; et al. Large-scale fluctuations in Precambrian atmospheric and oceanic oxygen levels from the record of U in shales. *Earth Planet. Sci. Lett.* **2013**, *369–370*, 284–293. [CrossRef]
85. McLennan, S.; Hemming, S.; Taylor, S.; Eriksson, K. Early Proterozoic crustal evolution: Geochemical and NdPb isotopic evidence from metasedimentary rocks, southwestern North America. *Geochim. Cosmochim. Acta* **1995**, *59*, 1153–1177. [CrossRef]
86. Nesbitt, H.; Young, G.M. Formation and diagenesis of weathering profiles. *J. Geol.* **1989**, *97*, 129–147. [CrossRef]
87. Gu, X.X.; Liu, J.M.; Zheng, M.H.; Tang, J.X.; Qi, L. Provenance and Tectonic Setting of the Proterozoic Turbidites in Hunan, South China: Geochemical Evidence. *J. Sediment. Res.* **2002**, *72*, 393–407. [CrossRef]
88. Hayashi, K.-I.; Fujisawa, H.; Holland, H.D.; Ohmoto, H. Geochemistry of $\sim$1.9 Ga sedimentary rocks from northeastern Labrador, Canada. *Geochim. Cosmochim. Acta* **1997**, *61*, 4115–4137. [CrossRef] [PubMed]
89. Girty, G.H.; Ridge, D.L.; Knaack, C.; Johnson, D.; Al-Riyami, R.K. Provenance and depositional setting of Paleozoic chert and argillite, Sierra Nevada, California. *J. Sediment. Res.* **1996**, *66*, 107–118. [CrossRef]
90. Floyd, P.A.; Leveridge, B.E. Tectonic environment of the Devonian Gramscatho basin, south Cornwall: Framework mode and geochemical evidence from turbiditic sandstones. *J. Geo. Soc. Lond.* **1987**, *144*, 531–542. [CrossRef]
91. Roser, B.P.; Korsch, R.J. Provenance signatures of sandstone-mudstone suites determined using discriminant function analysis of major-element data. *Chem. Geol.* **1988**, *67*, 119–139. [CrossRef]
92. Cullers, R.L.; Bock, B.; Guidotti, C. Elemental distributions and neodymium isotopic compositions of Silurian metasediments, western Maine, USA: Redistribution of the rare earth elements. *Geochim. Cosmochim. Acta.* **1997**, *61*, 1847–1861. [CrossRef]
93. Fedo, C.M.; Sircombe, K.N.; Rainbird, R.H. Detrital Zircon Analysis of the Sedimentary Record. *Rev. Mineral. Geochem.* **2003**, *53*, 277–303. [CrossRef]
94. Hu, J.; Wang, H.; Huang, C.Y.; Tong, L.X.; Mu, S.L.; Qiu, Z.W. Geological characteristics and age of the Dahongliutan Fe-ore deposit in the Western Kunlun orogenic belt, Xinjiang, northwestern China. *J. Asian Earth Sci.* **2016**, *116*, 1–25. [CrossRef]
95. Gao, X.F.; Xiao, P.X.; Kang, L.; Zhu, H.P.; Guo, L.; Xi, R.G.; Dong, Z. Origin of the Volcanic Rocks from the Ta'axi Region, Taxkorgan Xinjiang and Its Geological Significance. *Earth Sci.* **2013**, *38*, 1169–1182, (In Chinese with English abstract).
96. Bhatia, M.R.; Crook, K.A. Trace element characteristics of graywackes and tectonic setting discrimination of sedimentary basins. *Contrib. Mineral. Petrol.* **1986**, *92*, 181–193. [CrossRef]
97. McLennan, S.M.; Taylor, S.R.; McCulloch, M.T.; Maynard, J.B. Geochemical and Nd Sr isotopic composition of deep-sea turbidites: Crustal evolution and plate tectonic associations. *Geochim. Cosmochim. Acta* **1990**, *54*, 2015–2050. [CrossRef]
98. Bhatia, M.R. Plate Tectonics and Geochemical Composition of Sandstones. *J. Geol.* **1983**, *91*, 611–627. [CrossRef]
99. Bhatia, M.R. Rare earth element geochemistry of Australian Paleozoic graywackes and mudrocks: Provenance and tectonic control. *Sediment. Geol.* **1985**, *45*, 97–113. [CrossRef]
100. Frisch, W.; Meschede, M.; Blakey, R. Contractional theory, continental drift and plate tectonics. In *Plate Tectonics: Continental Drift and Mountain Building*; Frisch, W., Meschede, M., Blakey, R.C., Eds.; Springer: Berlin/Heidelberg, Germany, 2011; pp. 1–13.
101. Liu, C.J. *Composition and Tectonic Evolution of West Kunlun Orogenic Belt and Its Periphery in the Early Paleozoic-Early Mesozoic*; Chang'an University: Xi'an, China, 2015; (In Chinese with English abstract).
102. Liu, Z.; Jiang, Y.H.; Jia, R.Y.; Zhao, P.; Zhou, Q.; Wang, G.C.; Ni, C.Y. Origin of Middle Cambrian and Late Silurian potassic granitoids from the western Kunlun orogen, northwest China: A magmatic response to the Proto-Tethys evolution. *Mineral. Petrol.* **2014**, *108*, 91–110. [CrossRef]
103. Cui, J.T.; Wang, J.C.; Bian, X.W.; Zhu, H.P.; Yang, K.J. Geological characteristics of Early Paleozoic amphibolite and tonalite in northern Kangxiwar, West Kunlun, China and their zircon SHRIMP U-Pb dating. *Geol. Bull. China* **2006**, *25*, 1441–1449, (In Chinese with English abstract).

104. Liu, X.Q.; Zhang, C.L.; Zou, H.; Ye, X.T. Diverse metavolcanic sequences in the Cambrian accretionary complex at the Pamir Syntax: Implications for tectonic evolution from Proto-Tethys to Paleo-Tethys. *J. Asian Earth Sci.* **2023**, *241*, 105481. [CrossRef]
105. Ding, D.G.; Wang, D.X.; Liu, W.X.; Sun, S. *The Western Kunlun Orogenic Belt and Basin*; Geological Publishing House: Beijing, China, 1996; Volume 36, pp. 1–224. (In Chinese)